Surv Geophys (2017) 38:963–1004
https://doi.org/10.1007/s10712-017-9432-4

On Joint Modelling of Electrical Conductivity and Other Geophysical and Petrological Observables to Infer the Structure of the Lithosphere and Underlying Upper Mantle

J. Fullea[1]

Received: 28 November 2016 / Accepted: 21 September 2017 / Published online: 4 October 2017

Abstract This review paper focuses on joint modelling and interpretation of electromagnetic data and other geophysical and petrological observables. In particular, integrated geophysical–petrological modelling approaches, where the electrical conductivity and other physical properties of rocks are required to be linked by the common subsurface thermochemical conditions within a self-consistent thermodynamic framework, are reviewed. The paper gives an overview of the main geophysical electromagnetic techniques/data sets employed in lithospheric and mantle imaging including recent advances using satellite data, and an up-to-date summary of the most relevant laboratory experiments regarding the electrical conductivity of upper mantle minerals for various temperature–pressure–water conditions. The sensitivity of electrical conductivity and other geophysical parameters (density, seismic velocities) of mantle rocks to changes in temperature and composition are presented based on a Monte Carlo method parameter exploration. Finally, a case study in Central Tibet is presented where both seismological (long-period surface wave phase velocities) and electromagnetic (magnetotelluric) data—simultaneously including the constraints offered by topography, surface heat flow and mantle xenoliths—have been integrated. The modelling is based on a self-consistent petrological-geophysical thermodynamic framework where mantle properties are calculated as a function of temperature, pressure, and composition. The Tibetan case study offers an excellent opportunity to illustrate the different and complementary sensitivities of the various data sets used and to show how integrated thermochemical models of the lithosphere can help understand settings with a complex tectonic evolution.

Keywords Electrical conductivity · Integrated geophysical–petrological modelling · Lithosphere · Magnetotelluric · Seismics · Density · Mantle composition · Water content

✉ J. Fullea
jfullea@cp.dias.ie

[1] Dublin Institute for Advanced Studies, 5 Merrion Square, Dublin 2, Ireland

1 Introduction

The electrical conductivity of a material, σ (S/m), expresses the capacity of the medium to carry an electrical current. It is often also represented by its inverse, the resistivity, ρ (Ω m). The conductivity of the subsurface depends mostly on the in situ thermochemical conditions within the Earth, and therefore, imaging 3D conductivity variations by means of electromagnetic methods is a useful tool for a number of relevant topics in solid Earth sciences including the analysis of tectonically stable lithosphere (e.g., Korja 2007; Selway et al. 2014; Neska 2016), geodynamic modelling (e.g., Heise and Ellis 2016), or melt- and water-related processes in the upper mantle (e.g., Karato and Wang 2013; Yoshino and Katsura 2013; Khan 2016). There are two ways of deriving the electrical conductivity of Earth's rocks: (i) using indirect electromagnetic geophysical methods (e.g., Karato 2011; Siripunvaraporn 2012; Kuvshinov 2012, see Sect. 2.1) and (ii) conducting experimental studies directly on rock samples at controlled laboratory conditions (e.g., Yoshino 2010; Pommier 2014, see Sect. 2.2). Both electrical conductivity and its inverse, electrical resistivity, are referred to in the literature, with an emphasis on the former in laboratory measurements. Conversely, most electromagnetic (EM) surveys, particularly MT, report resistivity to avoid the small fraction ($\ll 1$) conductivity values. Both representations are equivalent, and I will employ them interchangeably throughout this paper.

There are two levels of parameterizations connecting Earth observations and models of the subsurface. On a first level we have the so-called secondary geophysical parameters (e.g., electrical conductivity) that relate to a particular Earth observation (e.g., electric and magnetic time series) through an appropriate physical theory (e.g., propagation of EM waves according to Maxwell equations). On a second and more fundamental level we have the primary parameters describing the thermochemical state of rocks within the Earth (e.g., temperature, composition, water, melts) that control the secondary geophysical parameters according to thermodynamics and mineral physics. Based on these two levels of parameterization, there are three main approaches to combine electrical conductivity and other geophysical and petrological data sets.

A first approach within the first level of parameterization consists of the comparison (either qualitative or quantitative) of 1D, 2D, or 3D conductivity models derived from electromagnetic modelling with other data sets (e.g., Kelbert et al. 2009; Spichak et al. 2013; Thiel and Heinson 2013; Ichiki et al. 2015, Jones et al. 2012; Le Pape et al. 2015). As noted by Heise and Ellis (2016), the absolute value of MT data has to be interpreted with caution in such joint studies as it could be over- or underestimated due to the choice of the initial model among other factors.

In the second approach, still within the first level of parameterization, some authors propose a combined inversion of EM and other data sets, e.g., MT and gravity (Jegen et al. 2009), MT and surface waves (Moorkamp et al. 2010; Roux et al. 2011; Mandolesi and Jones 2014), or MT and receiver functions (Moorkamp et al. 2007). In this second approach, EM and the other data are jointly inverted for the subsurface distribution of electrical conductivity and other physical properties of rocks (seismic velocity or density) that are either treated as decoupled, independent variables or linked by empirical relationships.

Finally, the third approach is the integrated geophysical–petrological modelling of EM and other data sets within a self-consistent thermodynamic framework (e.g., Khan et al. 2006; Fullea et al. 2011; Khan and Shankland 2012; Koyama et al. 2014; Vozar et al. 2014). Integrated approaches not only jointly account for EM and other geophysical data,

but also require the output models of electrical conductivity and other physical properties (i.e. the second level of parameterization) to be linked by the thermochemical conditions within the Earth. Integrated models, therefore, aim at imaging the ultimately relevant temperature, pressure, and compositional fields in depth, using electrical conductivity and other physical properties of rocks as a secondary parameter in the modelling process (see Sect. 3 for further details). In this review, I will focus on the third approach, integrated geophysical–petrological studies.

2 Electrical Conductivity in the Upper Mantle

2.1 Electromagnetic Geophysical Methods

The magnetotelluric (MT) method is a natural source electromagnetic method used to image the Earth from the near-surface (100 m) to deep within the mantle (> 100 km) depending on the frequency of the electromagnetic waves. Long-period MT responses cover periods up to few days and sample upper mantle depths. However, high-quality long-period MT data (periods < 10 days) are difficult to obtain due to technical and intrinsic limitations of the method (Shimizu et al. 2010; Semenov and Kuvshinov 2012; Koyama et al. 2014). MT is based on the relation between the temporal variations of the Earth's electric and magnetic fields, and its subsurface electrical resistivity structure (e.g., Jones 1999). The objective of MT modelling is to map the conductivity/resistivity distribution laterally and with depth by the inversion of the complex frequency-dependent impedance tensor responses that are usually displayed as apparent resistivities and phases.

Traditionally, deep EM studies have used time series of the magnetic field variations recorded on the global network of geomagnetic observatories to infer the Earth's electrical conductivity. 1D geomagnetic deep soundings and horizontal spatial gradient studies (e.g., Fujii and Schultz 2002), and 3D inversion of geomagnetic observatory data (e.g., Kelbert et al. 2009; Tarits and Mandéa 2010) constrain the conductivity distribution in the mantle in the depth range 400–1600 km (i.e. periods of few days to few months). Electromagnetic perturbations of ionospheric source (Sq) are sensitive to the lithosphere–uppermost mantle conductivity structure (depth 100–400 km, cf. Koch and Kuvshinov 2013). The ionospheric field is characterized by periods of a few hours and a complex spatial structure. When using global ground-based data, the Sq source is conventionally recovered using the potential method that allows for separating internal (induced field) and external (the source, inducing field) parts of the magnetic potential by exploiting the least squares technique and the spherical harmonic representation. Unfortunately, this separation cannot be applied to satellite data: as satellites orbit far above the ionospheric shell, the Sq signals are seen as purely internal and thus the separation of satellite Sq signals into internal and external parts is not possible (e.g., Schnepf et al. 2015). The main limitation of observatory data is their poor coverage of the Earth's surface (sparse distribution over continents and almost nothing over oceans) that severely hampers the robustness and accuracy of global EM models. Satellite measurements represent an attractive alternative to the sparse terrestrial observatory data, providing high-precision and high-resolution magnetic field measurements with uniform global coverage (e.g., Sabaka et al. 2004; Olsen et al. 2013). Recent advances in global 3D EM (spherical) forward modelling, the increasing availability of computational resources, and satellite data have made it possible to obtain a new generation of global electrical conductivity models of the mantle. The conductivity

structure in the lower mantle can be derived from the inversion of time series of internal (induced) and external (inducing) spherical harmonic expansion coefficients related to disturbed storm-time variations of magnetospheric ring current origin (Dst) (time and frequency approaches cf. Velímský 2013 and Püthe and Kuvshinov 2014).

The spatial gradients of the solar and lunar gravity fields produce ocean tides involving the motion of electrically conducting sea water. Such ocean electrical currents in the presence of an ambient main magnetic field produce secondary electric and magnetic fields. In contrast to Sq currents (induced field), ocean tides induce galvanic currents in physical contact with the electric media. Hence, whereas EM sensing based on Sq data (i.e. toroidal currents) illuminates well-conductive areas within the Earth (e.g., melt, volatiles), ocean tides (toroidal and poloidal currents) are comparatively more sensitive to resistive areas (e.g., Fainberg et al. 1990). The EM signals due to (periodic) tidal sources (lunar semidiurnal, M2, and lunar elliptic semidiurnal, N2) can be detected either at seafloor (Kuvshinov et al. 2006; Schnepf et al. 2014) or coastal stations (Maus and Kuvshinov 2004; Love and Rigler 2014). Recent studies suggest that satellite magnetic data could also be used to measure ocean tide currents (Schnepf et al. 2015; Grayver et al. 2016; Sabaka et al. 2016).

2.2 Mineral Physics: An Experimental Perspective

The major upper mantle mineral phases (e.g., olivine, pyroxenes, and garnet) show an insulator-like electrical behaviour at relatively low temperatures. However, in the temperature range prevalent in the upper mantle (i.e. 500 °C $< T <$ 1520 °C, e.g., Anderson 2000; Herzberg et al. 2007; Fullea et al. 2011, 2012, 2014; Khan et al. 2013; Kuskov et al. 2014), the electrical conductivity of the mantle minerals can be adequately described as an activated process, or processes, in a semiconductor and, therefore, following an Arrhenius-type power equation:

$$\sigma = \sigma_0 \exp\left(\frac{-\Delta H}{k_B T}\right) \tag{1}$$

where σ_0 (S/m) is a pre-exponential term, ΔH (eV) the activation enthalpy, T (K) the temperature, and k_B (eV/K) Boltzmann's constant. The activation enthalpy includes two terms: the activation energy, ΔU (eV), and an extra term that accounts for the pressure dependence:

$$\Delta H = \Delta U + P\Delta V \tag{2}$$

where ΔV (cm^3/mol) is the activation volume and P (GPa) the pressure. The conduction mechanism in this temperature range changes at around 1300–1550 °C from small polaron (electron hopping between ferric Fe^{3+} and ferrous Fe^{2+} ions) at $T <$ 1300 °C, to ionic conduction (charge carriers are magnesium vacancies) (e.g., Schock et al. 1989; Yoshino et al. 2008a). For olivine, a variation in the conduction regime from small polaron to ionic conduction has been reported at $T >$ 1300 °C (within the sublithosphere) (Schock et al. 1989; Constable 2006; Yoshino et al. 2009; Farla et al. 2010). For garnet, the small polaron to ionic conduction takes place at $T >$ 1530 °C (Yoshino et al. 2008b). In general, the ionic conduction shows an activation enthalpy typically $>$ 2 eV in olivine (Yoshino et al. 2009; Farla et al. 2010) and $>$ 1.6 eV in garnet (Yoshino et al. 2008b).

As expressed by Eq. (1), electrical conductivity is governed, to first order, by temperature variation. However, there are other variables (i.e. composition, partial melt, and/or

water content in the solid phase and the melt, see Sects. 2.2.1 and 2.2.2) that affect electrical conductivity to lesser or greater extent. It is well known that chemical substitution of magnesium by iron in the dodecahedral site of silicate minerals, without changes in the lattice symmetry, increases electrical conductivity (e.g., Hinze et al. 1981; Seifert et al. 1982; Omura et al. 1989; Romano et al. 2006). The amount of iron, either for the whole rock or for the individual mineral constituents, is usually described by the magnesium number, $\mathrm{Mg\#} = \mathrm{Mg}/(\mathrm{Mg} + \mathrm{Fe})$, or its converse, the iron content, $\mathrm{XFe} = 1 - \mathrm{Mg\#}/100$, where Mg and Fe refer to the molar concentrations of those elements.

Laboratory studies at the temperatures and pressures relevant to the upper mantle are essential to understand the electrical behaviour of the mantle mineral constituents in situ. Such measurements have been taking place since the 1960s; see the review of early work by Duba (1976), and other reviews over the last 30 years by Hinze (1982), Laštovičková (1991), Nover (2005), Yoshino (2010) and Pommier (2014). In recent years, considerable effort has been expended into designing suitable experiments to measure the electrical properties of many of the mantle minerals under various conditions (e.g., Wang et al. 2006; Dai and Karato 2009a, Yoshino et al. 2009; Yoshino and Katsura 2012; Karato 2011; Karato and Wang 2013). Fullea et al. (2011) presented a review of the state-of-the-art conductivity models for olivine, pyroxenes, and garnet, as the most representative minerals in the mantle down to the 410 km discontinuity (e.g., Ringwood 1975; Irifune and Ringwood 1987) including the Fe dependence. These authors proposed a model for the bulk electrical conductivity of the mantle that integrates temperature, pressure, and compositional variations according to available laboratory results. The equations describing the conductivity of mantle minerals include three terms:

$$\begin{aligned} \sigma &= \sigma_0 \exp\left(\frac{-\Delta H(X_{\mathrm{Fe}}, P)}{k_{\mathrm{B}} T}\right) + \sigma_{0i} \exp\left(\frac{-\Delta H_i}{k_{\mathrm{B}} T}\right) + \sigma_{\mathrm{p}} \\ \Delta H(X_{\mathrm{Fe}}, P) &= a + bX_{\mathrm{Fe}} + cX_{\mathrm{Fe}}^2 + dX_{\mathrm{Fe}}^3 + eX_{\mathrm{Fe}}^4 + fX_{\mathrm{Fe}}^5 + P\Delta V \end{aligned} \tag{3}$$

The first term in the first row of Eq. 3 describes conduction due to small polarons, and the second term represents the ionic conduction at high temperatures. The second row in Eq. 3 is the activation enthalpy for small polaron conduction, accounting for the iron content and pressure dependencies. All the experimentally derived parameters describing the conductivity model for each mineral (σ_0, σ_{0i}, a, b, c, d, e, f, ΔV, ΔH_i, ΔH_0, α, A, r) are listed in Table 1. A similar mineral physics database extended to include transition zone and lower mantle minerals is given by Khan and Shankland (2012) and Khan (2016). Figure 1 summarizes different experimental results for olivine, pyroxenes, and garnet for a 180-km-thick and chemically stratified lithosphere (mantle compositions as in Table 1 in Fullea et al. (2011)).

The third term in the first row of Eq. 3, the proton conduction (σ_{p}), describes the electrical conductivity contribution from hydrogen (OH) diffusion. This can be expressed as:

$$\sigma_{\mathrm{p}} = f(C_{\mathrm{w}}) \exp\left(\frac{-\Delta H_{\mathrm{wet}}(C_{\mathrm{w}})}{k_{\mathrm{B}} T}\right) \tag{4}$$

The proton term includes conduction from different chemical species in the crystal lattice and in the grain boundaries. It was first proposed by Karato (1990) that the presence of small amounts of water (part per million scales) in the form of protons structurally linked to oxygen in the so-called nominally anhydrous minerals (e.g., olivine and its high-pressure

Table 1 Small polaron and ionic conduction terms for the bulk conductivity model of the mantle adopted by Fullea et al. 2011

	log σ_0/log σ_{0i} (S/m)	a	b	c	d	e	f	ΔV (cm^3/mol)	ΔH_i (eV)
Ol[(1)]	2.4–3/4.73	1.642	0.246	−4.85	3.259	–	–	0.68	2.31
Opx[(2)]	2.4–3.72/–	1.9	−2.77	2.61	−1.09	–	–	–	–
Cpx[(3)]	3.25/–	2.075	−2.77	2.61	−1.09	–	–	–	–
Gnt[(4)]	(2.67–3.39) + log[1–0.044 P (GPa)]/4.96	2.6	−15.33	80.4	−194.6	202.6	−75	2.5	2.05

See Eq. 3 and the text for further details. (1) Olivine model based on Wang et al. (2006) + Omura et al. (1989) + Xu et al. (2000) + Yoshino et al. (2009). (2) Orthopyroxene model based on Dai and Karato (2009b) + Seifert et al. (1982) + Xu and Shankland (1999). (3) Clinopyroxene model based on Xu and Shankland (1999) + Seifert et al. (1982). (4) Garnet model based on Dai and Karato (2009a) + Romano et al. (2006)

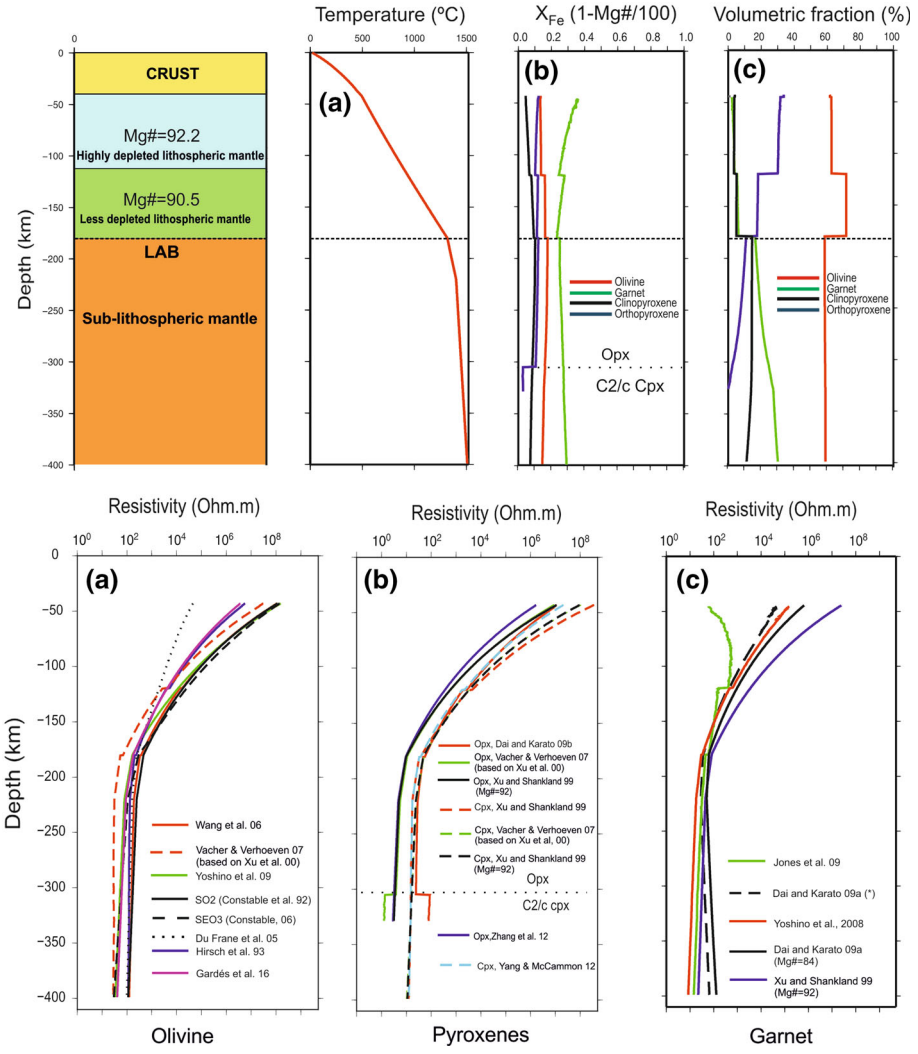

Fig. 1 Top panel: Reference lithospheric structure assumed to compare the electrical conductivity of mantle minerals according to different experimental results (see the text for further details). From left to right: temperature, iron content, and mineral assemblage distributions computed using the software LitMod (Fullea et al. 2009), see Sects. 3.1–3.3. Bottom panel: Comparison of different laboratory results for the electrical resistivity of olivine (**a**), pyroxenes (**b**), and garnet (**c**) under dry conditions (see the text for further details). Temperature, pressure, and iron content are taken from the reference lithospheric column in panel above. *Modified version of Dai and Karato's (2009b) garnet resistivity model including measurements for the activation enthalpy as a function of iron content [after Romano et al. (2006)]

polymorphs, pyroxenes, and garnet) could significantly enhance mineral conductivity. After this seminal work, a number of experimental studies on the topic have been published (e.g., Wang et al. 2006; Yoshino et al. 2009; Poe et al. 2010; Yang et al. 2012; Yoshino and Katsura 2012; Karato 2015). For various reasons, including different temperature–pressure and water content ranges and sample preparation, the results of these experiments are controversial (see, for example, Karato and Dai 2009; Yoshino 2010) yet

coincident in the observation that water considerably increases electrical conductivity of nominally anhydrous minerals. Jones (2016) discussed in detail the role that the different calibrations in the spectral techniques used to measure water content in rock samples may have played in this controversy. This author also claimed that, in the majority of the experiments conducted to date, the amount of water considered is far from the typical water contents measured in xenolith samples (see Sect. 2.2.1), thus potentially biasing the form of the equation used to fit the experimental measurements. As for the specific form of Eq. 4, there are two widely used parameterizations in the literature. The first parameterization (PC1) relies on the experimental results from Karato's and Dai's laboratories for olivine (e.g., Wang et al. 2006; Dai and Karato 2014a, b), orthopyroxene (Dai and Karato 2009b), and garnet (Dai and Karato 2009a; Dai et al. 2012, 2013) and is defined by a constant activation enthalpy in Eq. 4, ΔH_{wet}, and a pre-exponential term of the form: $f(C_w) = AC_w^r$. The second parameterization (PC2) follows the experimental results by Yoshino's and Poe's laboratories for olivine (e.g., Yoshino et al. 2009; Poe et al. 2010) and orthopyroxene (Zhang et al. 2012) and is defined by a water-dependent activation enthalpy (its cubic root) in Eq. 4, $\Delta H_{wet} = \Delta H_0 - \alpha C_w^{(1/3)}$, and a pre-exponential term of the form: $f(C_w) = AC_w$. Note that PC2 parameterization for proton conduction has also been used by Yang et al. (2011, 2012) to describe the electrical conductivity of lower crustal minerals. The non-unity value of r in the pre-exponential term $f(C_w)$ (Eq. 4) in PC1 is introduced to simulate the nonlinear effects due to multiple hydrogen atoms in a single defect (in PC2, this effect is neglected and hence $r = 1$). The parameter α (Eq. 4) within the activation enthalpy is equal to 1/3 in PC2, setting a dependence on water content in the activation enthalpy, whereas PC1 ignores this effect setting $\alpha = 0$. The parameters describing both PC1 (ΔH_{wet}, A, r) and PC2 (ΔH_0, A, α) proton conduction terms are listed in Table 2.

Table 2 Proton conduction term for the PC1 and PC2 models

	ΔH_{wet} (eV)	$\log_{10} A$ (S/m)	r	A (eV/(wt.%)$^{1/3}$)
Ol$^{(1)}$ (PC1)	0.9	3.1	0.62	0
Ol$^{(2)}$ (PC2)	1.19	2.35	1	1.1
Ol$^{(3)}$ (PC2)	0.92	1.9	1	0.16
Ol$^{(4)}$ (PC1 and PC2)	0.91	3.05	0.86	0.09
Ol$^{(5)}$ (PC2)	0.92	2.63	1	0.4
Opx$^{(6)}$ (PC1)	0.85	2.6	0.62	0
Opx$^{(7)}$ (PC2)	0.84	2.58	1	0.08
Opx$^{(8)}$ (PC1)	0.84	3.83	0.9	0
Cpx$^{(9)}$ (PC1)	0.74	3.56	1.13	0
Cpx$^{(10)}$ (PC1)	0.76	3.67	0.94	0
Gnt$^{(11)}$ (PC1)	0.725	2.29	0.63	0
Gnt$^{(12)}$ (–)	$0.75 - P * \Delta V$ (1.4 cm^3/mol)	1.75	0	0

See Eq. 4 and the text for further details. (1) Olivine data from Wang et al. (2006). (2) Olivine data from Poe et al. (2010). (3) Olivine data from Yoshino et al. (2009). (4) Olivine model from Jones et al. (2012). (5) Olivine model from Gardés et al. (2014) assuming Bell's calibration. (6) Orthopyroxene data from Dai and Karato (2009b). (7) Orthopyroxene data from Zhang et al. (2012). (8) Fe-rich lower crustal orthopyroxene data from Yang et al. (2012). (9) Fe-rich lower crustal clinopyroxene data from Yang et al. (2011). (10) Fe-rich clinopyroxene (augite) data from Yang and McCammon (2012). (11) Garnet data from Dai and Karato (2009a). (12) Garnet data (wet with 465 wt ppm) from Dai et al. (2012)

Different attempts have been made on various grounds to overcome the discrepancies between PC1 and PC2. Jones et al. (2012) use high-quality MT data and other geochemical constraints in the Kaapvaal craton (South Africa) to recalibrate the parameters in Eq. 4 for olivine within the water content range expected from xenolith measurements, i.e. 60–100 wt ppm (Table 2 and see Sect. 2.2.1). These authors found that neither PC1 nor PC2 was able to reproduce MT field data in Kaapvaal and proposed a combination of PC1 and PC2 with modified parameters in Eq. 4 to match MT data. Another recent attempt to match all experimental data is the work by Gardés et al. (2014). These authors propose a conductivity law of the form of Eq. 3 (first row) accounting for small polaron, magnesium vacancies, and proton conduction with parameters tuned to match all available laboratory data. Gardés et al. (2014) assumed large errors (factor 4 compared to original estimates) to account for both bias and random errors in water content measurements from literature. The proton conduction term in Gardés et al. (2014) model assumes the parameterization of PC2 (i.e. $r = 1$ and $\alpha \neq 0$) (Table 2). Figure 2 summarizes the resulting electrical conductivity for a 180-km-thick and lithospheric geotherm (see Fig. 1 for details) for the different proton conduction models.

An alternative approach to estimate the electrical conductivity of minerals is using the Nernst-Einstein equation relating the concentration of the charge carrier and the diffusivity of the charge carrier to electrical conductivity. Hydrogen is the chemical species that diffuses the fastest (by orders of magnitude) in olivine (e.g., Chakraborty 2010; Demouchy and Bolfan-Casanova 2016). Diffusion includes two processes: volume diffusion within a phase and boundary diffusion. In the context of proton diffusion in olivine, this translates

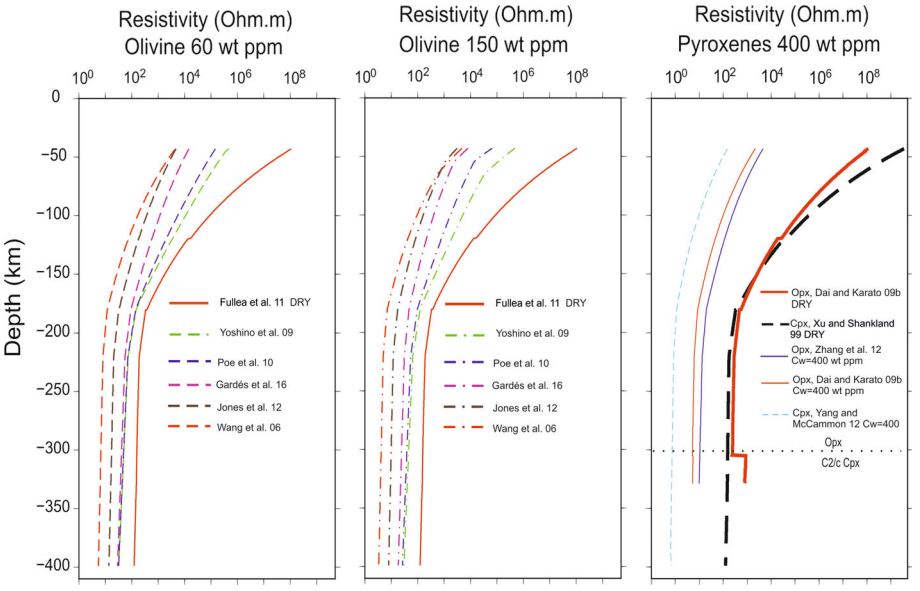

Fig. 2 Comparison of different laboratory results examining the effect of water content on electrical resistivity (i.e. the proton conduction term in Eq. 4, see the text for further details) of (from left to right): olivine at 60 wt ppm (left), olivine at 150 wt ppm (centre), and pyroxenes at 400 wt ppm (right). Temperature, pressure, and iron content are taken from the reference lithospheric column of Fig. 1. The water content distribution with depth is assumed to be constant throughout the whole upper mantle. Solid lines are dry resistivity depth profiles for olivine (left and centre). For the pyroxenes (right), the thick solid and dashed lines are dry resistivity for orthopyroxene and clinopyroxene, respectively

into grain and grain boundary diffusion. Grain boundary diffusion of hydrogen in olivine is orders of magnitude faster than volume diffusion (Demouchy 2010). The ratio between volume and grain boundary diffusion depends on grain size. Jones (2016) estimated that for a 1-nm-thick grain boundary, the grain boundary diffusion will overcome volume diffusion up to a grain size of 0.1–1 mm. Based on the work of Demouchy (2010) and ten Grotenhuis et al. (2004), Jones (2016) proposed a conductivity model for olivine including small polaron, proton, and ionic contributions including grain boundary effects for the latter two terms. The grain size dependence in his formulation allowed Jones (2016) to estimate this parameter for the interconnected most conducting phase in two locations within Kaapvaal craton based on conductivity values derived from high-quality MT data (Jones et al. 2009b). The expected grain size found by Jones (2016) from conductivity models and estimated temperatures from xenoliths (see Jones et al. 2012) is 2–3 orders of magnitude smaller than the measured grain sizes from in situ xenoliths (i.e. 5–12 mm, Lallemant et al. 1980).

Temperature is in general the most important parameter controlling the electrical conductivity of mantle minerals as illustrated in the example from Fig. 1: the imposed chemical boundaries at 120 km depth and at the base of the lithosphere (180 km) in the model produce only minor changes in conductivity compared to the change in the slope from the thermally conductive domain (steep) to the convective one (gentle). Under some conditions (i.e. small grain size), proton conduction related to water is the dominant process (Fig. 2). The presence of melt can also significantly enhance the conductivity of minerals provided the required connectivity (see Sect. 2.2.2). The amount of iron is only relatively important in the case of high iron content variations. Pressure does not have an appreciable effect in the conductivity of pyroxenes (Dai et al. 2006), but is relevant for olivine (Xu et al. 2000) as well as for garnet (Dai and Karato 2009a) in the sublithospheric mantle ($T > 1300$ °C) (Fig. 1). The effect of oxygen fugacity on the conductivity of mantle minerals is only of minor importance in comparison with temperature or iron content, particularly in view of the uncertainties in the EM data used to infer subsurface electrical conductivity (e.g., Jones et al. 2009a; Khan 2016).

2.2.1 Proton Conduction: Water Distribution in the Mantle

The presence of water (i.e. OH defects) dissolved in mantle rocks can significantly enhance electrical conductivity of mantle minerals (e.g., Karato 1990; Wang et al. 1999, 2006; Yoshino et al. 2009; Poe et al. 2010). The actual amount of water in the mantle remains debated (see, for example, Demouchy and Bolfan-Casanova 2016), but of interest as its presence dramatically affects mantle viscosity, a key parameter in geodynamic evolutionary models. There are two end-member cases defining water content in the mantle: (i) experimental measurements of OH defects in minerals either using secondary ion mass spectrometry (SIMS) or Fourier transform infrared spectroscopy (FTIR) and (ii) experimental measurements of water storage capacity at high pressure under water-saturated conditions. As for direct measurements of water, it is worth mentioning that due to decompression experienced by mantle xenoliths brought up to the surface, water can diffuse out of the sample (i.e. into grain boundaries space) (Demouchy 2010). Water diffusion out seems to be relevant for garnet and, to a lesser extent, for olivine (Demouchy et al. 2006). Hence, directly measured water contents in xenolith should be considered as the minimum possible values. The absorption of additional water into a xenolith rock due to re-equilibration with a water-saturated melt on its way to the surface is possible, but unlikely (e.g., Demouchy and Mackwell 2006). Water storage capacity or water solubility

in a mineral is the maximum possible water content that a mineral, or an assemblage of minerals, can accommodate within their structures without saturating or producing a water-rich fluid or hydrous melt at a given pressure. The amount of water in the mantle is bounded on the low side by the measured water content in xenolith and peridotite massif samples (e.g., Demouchy and Bolfan-Casanova 2016) and on the high side by the water solubility (e.g., Zhao et al. 2004) falling most likely close to the xenolith measurements (see Figs. 3 and 4).

Zhao et al. (2004) conducted an experiment on the solubility of hydrogen (i.e. the water storage capacity, $C_{\mathrm{OH}}^{\mathrm{ol}}$) in synthetic forsterite and San Carlos olivine at temperatures between 1000 and 1300 C and a pressure of 300 MPa. Their results show that $C_{\mathrm{OH}}^{\mathrm{ol}}$ increases systematically with increasing temperature, with increasing water fugacity, and with increasing iron content (Zhao et al. 2004):

$$C_{\mathrm{OH}}^{\mathrm{ol}} = A f_{\mathrm{H_2O}} \exp\left(\frac{-(\Delta E^0 + P\Delta V^0) + \gamma X_{\mathrm{Fe}}}{RT}\right) \tag{5}$$

where $A = 5.62 \times 10^3$ wt ppm/GPa, $f_{\mathrm{H_2O}}$ is the water fugacity (GPa), $\Delta E^0 = 50$ kJ/mol, $\Delta V^0 = 10$ cm^3/mol, $\gamma = 97$ kJ/mol, and R is the universal gas constant. Zhao et al. (2004) assumed a $f_{\mathrm{H_2O}}$ for pure water from Pitzer and Sterner (1995) formula, hence without accounting for any dissolved oxides in the vapour phase (Bali et al. (2008)). The water contents used in Eq. 5 assume the calibration of Patterson (1982) increased by a factor of 3.5 based on the calibration of Bell et al. (2003). Kohlstedt et al. (1996) determined water storage capacity in olivine at $T = 1100$ C and pressures up to 13 GPa using FTIR spectroscopy and Paterson calibration. This was later re-evaluated by Hirschmann et al. (2005)

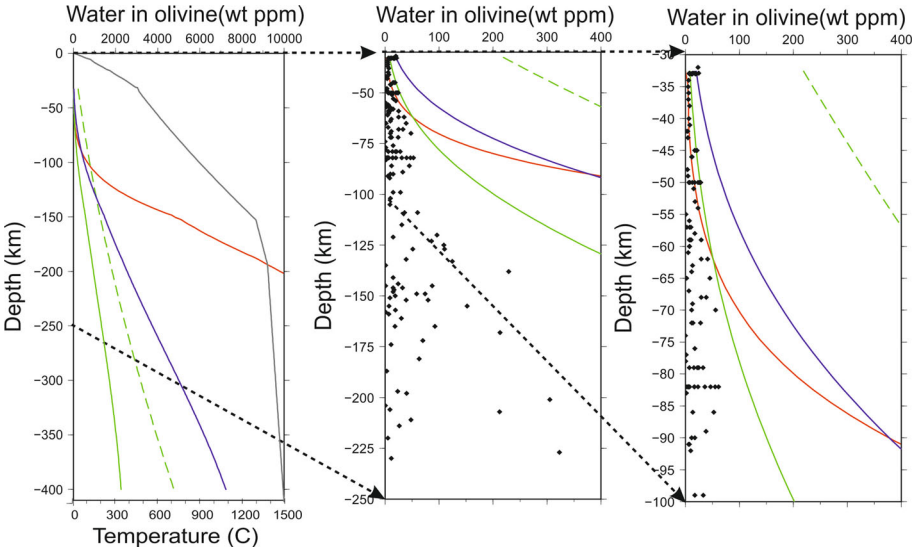

Fig. 3 Experimental water solubility curves for olivine. From left to right the vertical scale changes: down to 400 km (left), 250 km (centre), and 100 km (right). The different lines throughout the figure are: solid green (Kohlstedt et al. 1996); dashed green (Hirschmann et al. 2005); solid blue (Mosenfelder et al. 2006); and solid red (Zhao et al. 2004). See the text for further details. The black diamonds are natural sample olivine water contents from Demouchy and Bolfan-Casanova (2016) database. The grey solid line in the left plot is the geotherm used to compute the solubility curves

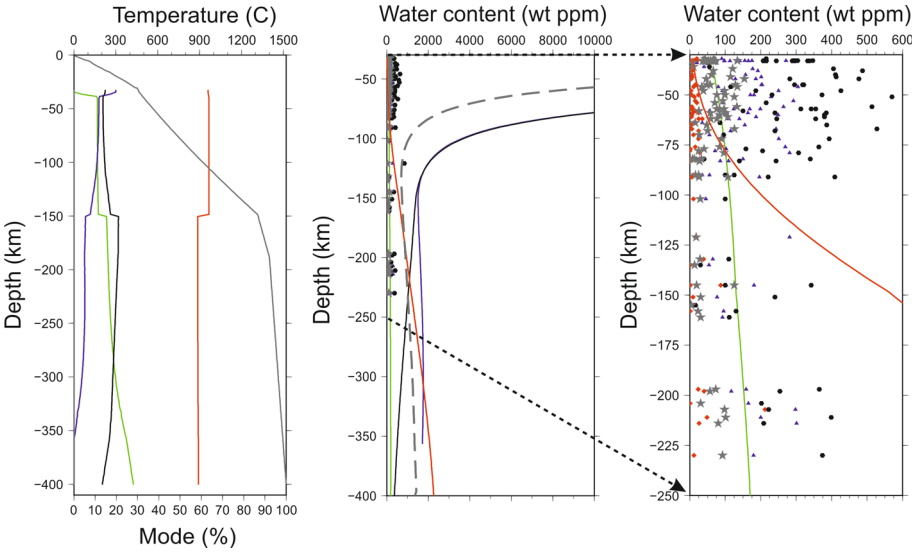

Fig. 4 Experimental water solubility curves for upper mantle minerals. Left plot: temperature distribution (solid grey) and volumetric fractions of the different minerals (red for olivine, green for garnet, blue for orthopyroxene, and black for clinopyroxene) assumed to compute experimental solubility curves (centre and right plots in the figure) and the bulk rock solubility (centre). The assumed bulk composition corresponds to an average garnet peridotite (column 1 in Table 4). Centre and right plots: water solubility for the different minerals according to various experimental results (solid red for olivine according to Kohlstedt et al. (1996), solid green for garnet according to Lu and Keppler (1997), solid blue orthopyroxene, and solid black clinopyroxene after Mierdel et al. (2007) and Gavrilenko (2008)) and natural rock water contents from Demouchy and Bolfan-Casanova (2016) database (red diamonds are olivine, blue triangles orthopyroxene, black hexagons clinopyroxene, and grey stars bulk rock). The vertical scale in the centre and right plots varies: down to 400 km (centre) and to 250 km (right). The absorption coefficients assumed for olivine, garnet, and the pyroxenes, for both the water content measurements and the solubility models are those of Bell et al. (1995, 2003)

based on the more accurate calibration of Bell et al. (2003) including also a constraint at 0.3 MPa from Bai and Kohlstedt (1993). Hirschmann et al. (2005) derived the following depth-dependent equation for the water storage capacity in olivine, C_{OH}^{ol} (in wt ppm):

$$\log_{10} C_{OH}^{ol} = (a + b \cdot z^{c}) \tag{6}$$

where, $a = -1.194$, $b = 2.263$, $c = 0.128$ and z is the depth in km.

Mosenfelder et al. (2006) also conducted an experiment on OH solubility in Fe-bearing olivine at temperatures between 1000 and 1300 C but in contrast to the experiment conducted by Zhao et al. (2004), where the pressure was 0.3 GPa, the pressure ranged from 2 to 12 GPa. These authors presented the following formula for OH solubility in olivine:

$$C_{OH}^{ol} = A f_{H_2O} \exp\left(\frac{-P\Delta V^0}{RT}\right) \tag{7}$$

where $A = 2.45 \times 10^3$ H/10^{6}Si/GPa (149.8 wt ppm/GPa), f_{H_2O} is the water fugacity (GPa), $\Delta V^0 = 10.2$ cm^3/mol, and R is the universal gas constant (Mosenfelder et al. 2006). Using the same expression, Kohlstedt et al. (1996) (using the calibration of Patterson (1982)) derived the following parameters: $A = 1.1 \times 10^3$ H/10^{6}Si/GPa (67.3 wt ppm/GPa) and $\Delta V^0 = 10.6$ cm^3/mol.

The water capacity in olivine from the available laboratory results is shown in Fig. 3. The differences among the experimental results are evident at all upper mantle depths. At the top of the transition zone (olivine–wadsleyite, 13 GPa), the solubility according to Zhao et al. (2004) is around an order of magnitude larger than the estimates from the other laboratory studies: 32,510 wt ppm (Zhao et al. 2004) versus 2260–7245 wt ppm (Kohlstedt et al. 1996; Hirschmann et al. 2005; Mosenfelder et al. 2006). Zhao et al.'s (2004) model starts to diverge from the other models at depths > 100 km (Fig. 3). At shallower depths, $z < 100$ km ($P < 3$ GPa), the model by Hirschmann et al. (2005) predicts a water capacity 0.5–1 log units larger than the other experimental results. Excluding the model of Hirschmann et al. (2005), the water storage in olivine in the uppermost mantle remains quite modest and almost dry beneath the Moho (0.2–20 wt ppm at $\approx$ 30 km), reaching 100 wt ppm at depths of 60–80 km (Fig. 3). The models of Mosenfelder et al. (2006) and Kohlstedt et al. (1996) differ in the whole upper mantle range by a factor 2.5–3.2 (with higher water capacity in Mosenfelder et al. (2006)) which could be related to the different FTIR calibrations assumed. For the same OH calibration, Zhao et al.'s (2004) model predicts $C_{\mathrm{OH}}^{\mathrm{ol}}$ that are 20–80 wt ppm lower than Mosenfelder et al.'s (2006) down to 90 km, where their estimates coincide in a value of around 380 wt ppm (Fig. 3). As noted by Mosenfelder et al. (2006), the mechanisms by which hydrogen is incorporated in olivine at low and high pressures may be significantly different.

In the case of pyroxenes (orthopyroxene and clinopyroxene, opx and cpx, respectively), the water solubility ($C_{\mathrm{OH}}^{\mathrm{px}}$) shows two main sources: an aluminium-free contribution ($C_{\mathrm{o}}^{\mathrm{px}}$) and an aluminium-related contribution ($C_{\mathrm{Al}}^{\mathrm{px}}$) (Mierdel et al. 2007). This can be expressed as:

$$\begin{aligned} C_{\mathrm{OH}}^{\mathrm{px}} &= C_0^{\mathrm{px}} + C_{\mathrm{Al}}^{\mathrm{px}} \\ C_0^{\mathrm{px}} &= A f_{\mathrm{H_2O}} \exp\left(\frac{-(\Delta E^0 + P\Delta V^0)}{RT}\right) \\ C_{\mathrm{Al}}^{\mathrm{px}} &= A_{\mathrm{Al}} (f_{\mathrm{H_2O}})^{1/2} \exp\left(\frac{-\left(\Delta E_{\mathrm{Al}}^0 + P\Delta V_{\mathrm{Al}}^0\right)}{RT}\right) \end{aligned} \tag{8}$$

Mierdel et al. (2007) determined experimental parameters based on Eq. 8 for pure Al-free enstatite (opx): $A = 1.35 \times 10^2$ wt ppm/GPa, $\Delta E^0 = -4.56$ kJ/mol, $\Delta V^0 = 12.1$ cm^3/mol, and for opx coexisting with the corresponding aluminous phase (spinel or garnet): $A_{\mathrm{Al}} = 4.2$ wt ppm/(GPa)$^{1/2}$, $\Delta E_{\mathrm{Al}}^0 = -79.685$ kJ/mol, $\Delta V_{\mathrm{Al}}^0 = 11.3$ cm^3/mol. Gavrilenko (2008) estimated the Al-free parameters for pure diopside (cpx): $A = 1.85 \times 10^2$ wt ppm/GPa, $\Delta E^0 = -11.12$ kJ/mol, $\Delta V^0 = 14.62$ cm^3/mol. The absorption coefficients from Bell et al. (1995) calibration were assumed to determine the OH contents in the works by Mierdel et al. (2007) and Gavrilenko (2008).

The water solubility in garnet remains controversial, especially for relatively high pressures $P > 7$ GPa. Lu and Keppler (1997) studied the solubility of water in natural pyrope at $T = 1000$ °C for the oxygen fugacity associated with the Ni–NiO buffer:

$$C_{\mathrm{OH}}^{\mathrm{gt}} = A (f_{\mathrm{H_2O}})^{1/2} \exp\left(\frac{-(\Delta E^0 + P\Delta V^0)}{RT}\right) \tag{9}$$

Lu and Keppler (1997) determined experimental parameters for Eq. 9 assuming the calibration of Bell et al. (1995): $A = 18.09$ wt ppm/(GPa)$^{1/2}$, $\Delta E^0 = -14$ kJ/mol, $\Delta V^0 = 5.71$ cm^3/mol. Following Fullea et al. (2011), the original value of the pre-exponent A in Lu and Keppler (1997) (67.9 wt ppm/(GPa)$^{1/2}$), valid only for $T = 1000$ °C, has

been modified to account for the enthalpy of the reaction in Eq. 9. According to the laboratory study of Withers et al. (1998) on pyrope garnets, in the presence of excess SiO_2 at $T = 1000$ °C in the pressure range 2–13 GPa, the water solubility of garnet increases down to 5 GPa ($z = 160$ km) up to values of > 1000 wt ppm, decreasing subsequently to below the detection limit for $P > 7$ GPa ($z = 215$ km). In contrast, the work by Mookherjee and Karato (2010) shows that the solubility of pyrope-rich garnet at $T = 1100$–1200 °C and $P = 5$–9 GPa is > 1000 wt ppm for $P > 7$ GPa. In general, the solubility predicted by the model of Withers et al. (1998) is higher than that of Lu and Keppler's (1997) except for $z > 215$ km. The results by Mookherjee and Karato (2010) suggest that the solubility of garnet is systematically higher than that derived by Lu and Keppler (1997) for the whole lithospheric and sublithospheric mantle range. Regardless of which experimental result is considered, for depths > 220 km olivine is the most important potential water host due to its higher water solubility in comparison with the other minerals (Fig. 4).

It is estimated from measurements in various tectonic settings that the water content in upper mantle minerals typically goes from dry up to 80, 200 and 400 wt ppm, for olivine, orthopyroxene, and clinopyroxene, respectively (e.g., Grant et al. 2007; Peslier 2010; Peslier et al. 2010; Baptiste et al. 2012; Doucet et al. 2014; Peslier and Bizimis 2015; Demouchy and Bolfan-Casanova 2016). Garnet shows the largest range of variations in water content from > 1000 wt ppm in ultra-high pressure (UHP) metamorphic rocks (Xia et al. 2005) to < 20 wt ppm in peridotites and eclogites in mantle xenoliths (Bell and Rossman 1992). Hirschmann (2006) estimated a bulk water content in the upper mantle, disregarding plumes or subduction zones, of 50–200 wt ppm range. Peridotite xenoliths studies in a well-studied craton in South Africa (Kaapvaal) show olivine water content estimates decreasing with depth, over the depth range from $P = 4$ GPa ($z = 130$ km) to $P = 6$ GPa ($z = 190$ km) (Peslier 2010; Peslier et al. 2010; Baptiste et al. 2012). At $P < 3.0$ GPa, the olivine samples in the Kaapvaal xenoliths seem to have lost their initial water content due to diffusion processes (Peslier and Luhr 2006). Both clinopyroxene and orthopyroxene in the Kaapvaal xenolith suite show a minimum water content at $P = 2.5$ GPa ($z = 80$ km), increasing down to 4.0–4.5 GPa ($z = 130$–140 km) and remaining constant with around 400 and 200 wt ppm, respectively, at $P > 4.5$ GPa (Peslier 2010).

Water contents measurements in garnet from peridotite and eclogite rocks in xenoliths show < 20 wt ppm in general, whereas Cr-poor garnet megacrysts are slightly wetter on average (33 wt ppm) (Bell and Rossman 1992). After filtering the samples from the Kaapvaal suite, Peslier (2010) found that garnet at $P > 4.5$ GPa is virtually dry (< 1 wt ppm). Grant et al. (2007) found similar water contents for the pyroxenes but significantly lower values for olivine (< 10 wt ppm) in samples from South African kimberlite pipes. In a recent work Demouchy and Bolfan-Casanova (2016) review published hydrogen content in a variety xenolith samples across the world (see their Table 2 for details). The water contents from Demouchy and Bolfan-Casanova (2016) are plotted in Figs. 3 and 4 along with experimentally determined solubility for different minerals. With the exception of a few shallow samples (< 35 km depth), olivine water content in natural olivine is bounded by the experimental solubility (e.g., Zhao et al. 2004; Kohlstedt et al. 1996) and ranges from dry to the water-saturated curve for depths up to 70 km (Fig. 3). At greater depths, water in olivine is much lower than the experimentally derived water storage capacity. As noted by Demouchy and Bolfan-Casanova (2016), there seems to be no significant differences between the water content of lherzolites (fertile) and harzburgites (depleted) in either the spinel (shallow) or garnet (deep) stability field, suggesting that

there is no apparent correlation between melt depletion and water content in olivine. Below 80 km, the hydrogen content in olivine seems to decrease down to around 100 km (local minimum) and then increases again (> 100 wt ppm) down to the deepest recorded xenolith measurements compiled in Demouchy and Bolfan-Casanova (2016) (230 km) (Fig. 3). Therefore, garnet peridotites are on average more hydrated than spinel peridotites. If the pyroxenes and garnet are taken into account, then the bulk water content of the xenoliths can be calculated (Fig. 4). The distribution of water in the pyroxenes follows a similar pattern than in olivine with a minimum around 120–130 km depth and then increasing progressively and in general well below the saturation values. The bulk water content mimics the variations in both the olivine and the pyroxenes modulated as well by the modal distribution. In the spinel stability field (< 70 km), the bulk water content varies between 50 and 100 wt ppm in agreement with estimates for a mid-ocean ridge basalt (MORB) mantle source (e.g., Hirschmann 2006). In the garnet stability field, the bulk water decreases with a minimum around 120–130 km depth and then increasing again to values of $\approx$ 100 wt ppm (Fig. 4).

The bulk amount of water in upper mantle peridotites is to a large extent controlled by the storage capacity in olivine (Ferot and Bolfan-Casanova 2012). In that sense, an important parameter is the so-called mineral/mineral water partition coefficients expressing how water is differently distributed among mantle minerals. The bulk rock water content, C_w, can be expressed as:

$$C_w = \sum\nolimits_{i=\text{phases}} C_w^i X^i \tag{10}$$

where C_w^i and X^i are the water content and modal amount of phase i (olivine, orthopyroxene, clinopyroxene, and garnet in the case of the upper mantle), respectively. Alternatively, C_w can be expressed in terms of the water partition coefficients $D_{H_2O}^{i/ol}$:

$$C_w = C_w^{ol}\left(X^{ol} + \sum_{i=\text{opx,cpx,gnt}} D_{H_2O}^{i/ol} X^i\right) \tag{11}$$

The partition coefficients are in general less prone to strong pressure and temperature variations than measurements of peridotite-saturated storage capacity (Hirschmann et al. 2009; Tenner et al. 2012) and that makes them useful for modelling purposes. In addition, partition coefficients allow redefining the variable space using only water content in olivine as a free parameter (e.g., Vozar et al. 2014; Khan 2016). Measurements made on mantle xenoliths and laboratory studies at controlled conditions show a range of partition coefficients (Table 3).

In the case of the pyroxenes, the partition between clinopyroxene and orthopyroxene, $D_{H_2O}^{cpx/opx}$, seems to be rather independent of compositional or pressure variations, with values of 1.7–2.2 in studies on natural peridotite samples, and of 1.4–3.5 in laboratory studies (Table 3). The dispersion is far wider in the case of the partitioning between olivine and pyroxenes. The amount of Al_2O_3 oxide in orthopyroxene seems to control the amount of water that the mineral can host (e.g., Grant et al. 2007; Mierdel et al. 2007; Ardia et al. 2012; Sakurai et al. 2014). For higher Al_2O_3 contents, orthopyroxene can host comparatively more water, and therefore, $D_{H_2O}^{ol/opx}$ decreases its value (Ardia et al. 2012; Sakurai et al. 2014). Grant et al. (2007) obtained similar results from analysis of natural samples observing a significant increase in $D_{H_2O}^{ol/opx}$ across the spinel–garnet stability field (Table 3).

Table 3 Partition coefficients for water in different upper mantle minerals

	$D_{H_2O}^{ol/opx}$	$D_{H_2O}^{cpx/opx}$
Sakurai et al. (2014)[a]	0.5–1 (Al_2O_3-free)	–
	0.24–2 ($Al_2O_3 < 1$ wt.%)	
	0.028–0.14 ($Al_2O_3 > 1$ wt.%)	
Novella et al. (2014)[b]	0.53	1.7
Ardia et al. (2012)[c]	$\left(2.63 * C_{Al_2O_3}^{opx} + 0.78\right)^{-1}$	–
Tenner et al. (2012)[d]	0.74	–
Kovácks et al. (2012)[e]	0.15–0.21	2.7–3.5
Ferot and Bolfan-Casanova (2012)[f]	0.92–3.6 (Al_2O_3-free)	–
	0.6 ($P = 2.5$ GPa, Al_2O_3)	
	1.11 ($P \geq 5$ GPa, Al_2O_3)	
Aubaud et al. (2004)[g]	0.11	1.4
Peslier (2010)[h]	0.37	1.76
Grant et al. (2007)[i]	0.011 (spinel field)	2.1
	0.085 (garnet field)	
Bell et al. (2004)[j]	–	2
Peslier et al. (2002)[k]	–	2.2
Demouchy and Bolfan-Casanova (2016)[l]	0.02–0.2 (spinel field)	2.1
	0.02–0.48 (garnet field)	

[a] Laboratory study at $P = 1.5$–6 GPa

[b] Laboratory study at $P = 6$ GPa, $T = 1400$ C

[c] Laboratory study at $P = 5$–8 GPa, $T = 1400$–1500 C

[d] Laboratory study at $P = 10$–13 GPa, $T = 1350$–1450 C

[e] Laboratory study at P = 2.5–4 GPa

[f] Laboratory study at $P = 2.5$–9 GPa, $T = 1175$–1400 C

[g] Laboratory study at $P = 1$–2 GPa, $T = 1230$–1380 C

[h, i, j, k, l] Natural sample water content measurements

Interestingly, the increase in $D_{H_2O}^{ol/opx}$ observed by Grant et al. (2007) in the garnet field, where less Al_2O_3 is available for the orthopyroxene phase, is due to a different mechanism by which water is incorporated into olivine (i.e. more water in garnet peridotites than spinel peridotites) rather than to a change in orthopyroxene's water content with depth. The partition coefficient values for olivine and orthopyroxene found by Grant et al. (2007) based on the analysis of eight natural samples from six geographic localities representing a variety of tectonic setting are rather low ($D_{H_2O}^{ol/opx} = 0.01$ and 0.085 for the spinel and garnet stability fields, respectively) compared with the values obtained from a larger data set compilation of mantle-derived rocks by Peslier (2010) (average $D_{H_2O}^{ol/opx}$ of 0.37, Table 3). Most of the samples in Peslier (2010) are from cratonic settings (with a significant bias towards the Kaapvaal craton) and exhibit average olivine water content larger than that reported by Grant et al. (2007) with similar values for the water contents in the pyroxenes in the two studies.

A more recent compilation by Demouchy and Bolfan-Casanova (2016) also shows comparatively larger maximum values of $D_{H_2O}^{ol/opx} = 0.2$ and 0.48 for the spinel and garnet stability fields, respectively (Table 3). Laboratory estimates of $D_{H_2O}^{ol/opx}$ indicate an increase with depth (for a decrease in Al_2O_3 available for orthopyroxene) (Ardia et al. 2012; Sakurai et al. 2014) also reported in xenolith-based studies (Grant et al. 2007; Demouchy and Bolfan-Casanova 2016). However, water content measurements in mantle xenoliths for the Kaapvaal craton show a systematic decrease in olivine water with depth (Peslier et al. 2010; Baptiste et al. 2012), resulting in the opposite behaviour (i.e. $D_{H_2O}^{ol/opx}$ decreasing with depth below 130 km). The work by Demouchy and Bolfan-Casanova (2016) includes samples from a cratonic setting in Siberia (data from Doucet et al. 2014) that, in contrast to xenoliths from the Kaapvaal craton (Peslier et al. 2010; Baptiste et al. 2012), exhibit high olivine water contents at depths $>$ 150 km that would lead to an increase in $D_{H_2O}^{ol/opx}$ across the spinel–garnet phase transition (Figs. 3 and 4). However, water content estimates in olivine inclusions within cratonic diamonds in Siberia, from the same locality as the xenoliths analysed by Doucet et al. 2014, show very low values of 0.5–5 wt ppm (Novella et al. 2015). This apparent contradiction suggests a rehydration process taking place after the diamond formed due to an interaction with either the kimberlitic magmas or metasomatic fluids/melts (Demouchy and Bolfan-Casanova 2016). The question whether these metasomatic interactions postdating to the Siberian craton formation conditions (as recorded and preserved in the diamond inclusions) affect large portions of the Archaean mantle or only local veins related to the kimberlitic magmatism remains open.

The presence of dissolved water is also a potential source of significant and observable electrical anisotropy. Dry undeformed olivine single crystals are only weakly anisotropic (e.g., Du Frane et al. 2005), but the presence of water can increase anisotropy by as much as one order of magnitude for 1000 wt ppm according to laboratory results (Poe et al. 2010). If proton conduction in olivine single crystals is adequately described by the Nernst-Einstein equation, then the conductivity should be proportional to the diffusivity of protons in olivine (e.g., Murch 1983; Jones 2016). The diffusion of protons in the olivine lattice is a process dominated by the interaction of protons with polarons at temperatures $<$ 900 °C and by the proton–metal vacancy interaction at temperatures $>$ 900 °C (e.g., Kohlstedt and Mackwell 1998; Demouchy and Mackwell 2006). Both the low- and the high-temperature diffusion regimes are strongly anisotropic, but in both regimes, the fast diffusion axis seems to be at odds with the high electrical conductivity axis in olivine observed in the most recent and detailed laboratory measurements at pressure above 6 GPa (Poe et al. 2010). Deformation seems to play an important role in electrical anisotropy (e.g., Gatzemeier and Tommasi 2006; Caricchi et al. 2011; Zhang et al. 2014; Pommier et al. 2015). Strongly sheared and deformed olivine samples show electrical anisotropy factors around ten, with the enhanced conductivity directed along the shear direction likely due to grain size reduction via dynamic recrystallization (Pommier et al. 2015). Moreover, macroscopic anisotropy in olivine (or other mineral phase) aggregates requires significant alignment of the single crystals, i.e. crystal or shape preferred orientation produced by dislocation creep mantle deformation (e.g., Gatzemeier and Tommasi 2006).

2.2.2 *Melt Conduction*

Another factor that can potentially enhance electrical conductivity of upper mantle minerals is the presence of an interconnected melt in the crust, lithospheric or sublithospheric

mantle. EM studies have identified partially molten zones associated with a very high conductivity (> 0.1 S/m) that cannot be explained by thermal or other effects (e.g., Baba et al. 2010; Heise et al. 2007; Toffelmier and Tyburczy 2007; Didana et al. 2014). The conductivity of various types of melts has been measured in several laboratory studies (see the review by Pommier 2014). Silicate melts, either rhyolitic (Gaillard 2004), dacitic (Laumonier et al. 2014), or basaltic (Tyburczy and Waff 1983; Ni et al. 2011; Miller et al. 2015), are about an order of magnitude less conductive than carbonatite melt (Gaillard et al. 2008; Yoshino et al. 2010; Sifré et al. 2014). In addition, the connectivity of carbonatite melt is larger than that of silicate melt (e.g., Hammouda and Laporte 2000). The conductivity of silicate melts has been shown to depend strongly on its chemical composition: amounts of Na, Si, and water content are the most important factors (e.g., Pommier et al. 2008; Ni et al. 2011). The effective conductivity of a partially molten rock depends on the conductivities of the bulk rock and melt, the melt fraction and the mixing rule connecting the bulk rock and the melt assumed. For the mixing rule, there are different options: Archie's law, cubic grains approach (Waff 1974), Hashin and Shtrikman maximum bound (Hashin and Shtrikman 1963). For a more detailed discussion of the fluid–rock mixing rules, the reader is referred to Glover (2010) and Laumonier et al. (2017). According to a recent experimental study by Pommier et al. (2015), a melt phase also induces significant electrical anisotropy in sheared olivine samples up to temperatures of 900 C, decreasing for higher temperatures. Interestingly, such temperature-driven behaviour indicates that the crystal or shape preferred orientation induced by deformation (responsible for seismic anisotropy) may differ from the melt preferred orientation (one of the possible causes for electrical anisotropy along with water) which would be controlled by melt–solid interfacial energy (Pommier et al. 2015). Thus, obliquity between seismic and electrical anisotropy not only could be due to large-scale geoelectric structure or crystal mineral orientations (e.g., Wannamaker 2005; Adetunji et al. 2015) but also could be related to the thermal regime via melt as exemplified by Pommier et al. (2015) in three Pacific Ocean settings.

The existence of a molten phase in the crust and upper mantle is dictated by the solidus curve of the different constituent rocks (e.g., Hirth and Kohlstedt 1996; Asimow et al. 2004; Katz et al. 2003). The solidus of lithospheric and upper mantle rocks is significantly decreased by the presence of even small amounts of water which in turn increases strongly the electrical conductivity of upper mantle rocks by proton diffusion (see Sect. 2.2.1). Therefore, both water and melt affect the conductivity of rocks in a nonlinear, entangled manner which thus makes it difficult to straightforwardly translate conductivity values from EM models into, for example, melt fraction estimates.

2.3 Sensitivity of Electrical Conductivity, Density and Seismic Velocities on the Thermochemical Structure

In Sect. 2.2, I have summarized the main characteristics of the electrical conductivity of minerals from an experimental, laboratory perspective. In the following, I explore the dependence of electrical conductivity and other secondary geophysical parameters (density, seismic velocities) to variations in the thermochemical conditions. In other words, what is the sensitivity of secondary geophysical parameters to changes in primary parameters (temperature, composition). Afonso et al. (2013a) presented an illustrative example taking the electrical conductivity, density, and seismic velocity of a given mineral aggregate at given temperature and pressure conditions (peridotite sample at $P = 3$ GPa and $T = 900$ C) computed based on thermodynamics and mineral physics. The idea of this

theoretical exercise is to retrieve the major element chemistry and temperature exploring the compositional/thermal space based on a Monte Carlo method. In this way, the sensitivity of the different secondary geophysical parameters to the thermochemical conditions is assessed. This is of particular importance in the light of studies that try to infer the thermochemical structure of the Earth based on secondary parameter models of resistivity, density, or seismic velocities (e.g., Cammarano et al. 2003; Simmons et al. 2010; Thiel and Heinson 2013; Ichiki et al. 2015; Cammarano and Guerri 2017).

2.3.1 Composition

We first fix the temperature and analyse the range of compositions that are able to reproduce the target secondary parameters. If only electrical conductivity is considered (Fig. 5), a region of low residuals (i.e. target minus estimated conductivity) is observed in the compositional space, preferentially in areas of low MgO values. In the case of only inverting *Vp* or *Vs*, the subset of acceptable models with residuals lower than the experimental uncertainties cover most of the compositional variability observed in natural samples. *Vp* exhibits a larger sensitivity compared to *Vs* due to the higher sensitivity of the bulk modulus to Al_2O_3 changes compared to that of the shear modulus. For both *Vp* and *Vs*, the low residuals align along a trend from high MgO and low CaO and Al_2O_3 (harzburgites and dunites) to low MgO and high CaO and Al_2O_3 (lherzolites), reflecting trade-offs between modal (phase abundancies) and chemical effects (major oxide composition of the

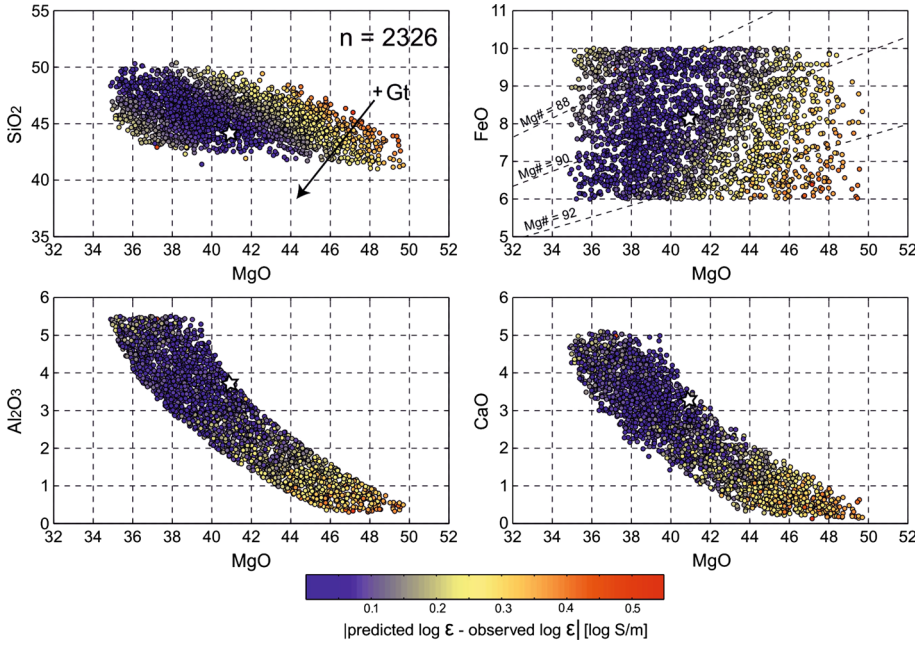

Fig. 5 Ensemble of 2326 acceptable compositions from a total random population of 2500 samples. The only constraining data are the bulk electrical conductivity. The true (target) composition is indicated by the white star (SiO_2 = 44.03, Al_2O_3 = 3.81, FeO = 8.08 and MgO = 40.82, CaO = 3.25 in wt.%), and the corresponding target electrical conductivity is $\log_{10}(\sigma/\sigma_0) = -3.9163$, with $\sigma_0 = 1$ S/m (calculated at $T = 900$ C, $P = 3$ GPa). The black arrow indicates the direction of increasing garnet content in the samples. The colour scale represents the misfit in absolute values. After Afonso et al. (2013a)

phases). The residuals using only bulk density are less extended along the MgO and FeO and SiO_2 axes although still define a large compositional range. Inverting together *Vp*, *Vs*, bulk density, and electrical conductivity allows to define a much narrower compositional space around the target composition compared to the case of inverting any of the secondary geophysical parameters alone (Fig. 6). Yet the low residuals lie along a linear trend in the compositional space from high MgO, low Al_2O_3, high FeO (harzburgites with anomalously high FeO and Al2O3 content) to low MgO, high Al_2O_3, low FeO (lherzolites with anomalously low FeO content). This linear trend, again, results from modal vs compositional effects. For example, typical harzburgites (from global databases) exhibit low density and high Vp and Vs, but FeO-rich harzburgites tend to host larger volumetric amounts of high density, low Vp, Vs olivine (fayalite). At the same time, relatively high amounts of Al_2O_3 promote more modal dense garnet phase, resulting in FeO- and Al_2O_3-rich harzburgites having similar physical properties than fertile lherzolites. Therefore, there is a trade-off between the influence on the secondary geophysical parameters of Mg# and FeO on the one hand, and of Al_2O_3 on the other hand. This modal-compositional trend is minimized at high pressures (depth > 300 km) as the capacity of the pyroxenes to incorporate Al_2O_3 (without generating more garnet, the densest, fastest, and more electrically conducting upper mantle mineral phase) is significantly reduced.

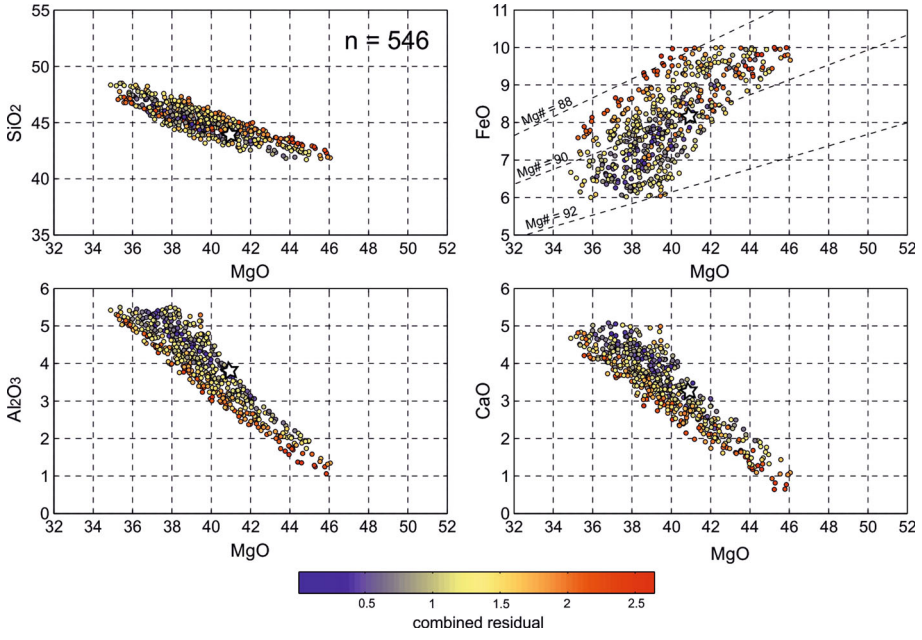

Fig. 6 Ensemble of 546 acceptable compositions from a total random population of 2500 samples. These acceptable samples simultaneously fit *Vs*, *Vp*, electrical conductivity, and bulk density constraints (within uncertainties). True (target) composition, *P–T* conditions, and corresponding σ as in Fig. 5. The corresponding target *Vs* and density are 4.634 km/s and 3378.79 kg/m^3, respectively (calculated at $T = 900$ C, $P = 3$ GPa). The colour scale represents the combined normalized residual. After Afonso et al. (2013a)

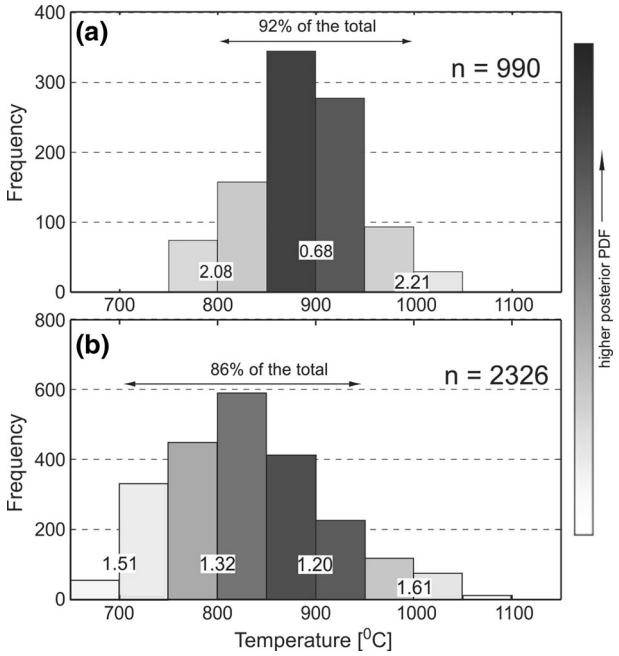

Fig. 7 Histogram of 990 samples that fit *Vp*, *Vs*, bulk density, and electrical conductivity within uncertainties. Note that more than 92% of these samples are found within the range 800 C $< T <$ 1000 C. **b** as in **a** but excluding electrical conductivity from the constraining parameters. The colour scale denotes values of the normalized posterior probability distribution function (PDF). Numbers between two temperature bins are the average residuals for the two adjacent bins. After Afonso et al. (2013a)

2.3.2 Temperature

Now we add temperature as a variable, in addition to composition, and try to retrieve the temperature and compositional values that reproduce the target secondary parameters (Fig. 7). If electrical conductivity is not included, the distribution of samples matching the target parameters is wider in temperature, i.e. the "true" temperature is less well defined. This fact reflects the higher sensitivity of conductivity (exponential) to temperature compared to that of seismic velocities or density (quasi-linear). However, due to its dependence on modal garnet and bulk MgO content, the electrical conductivity tends to produce wider low misfit compositional regions when added to seismic velocities and density inversions.

3 Integrated Geophysical–Petrological Modelling

Integrated modelling of geophysical–petrological data sets (e.g., gravity, seismic, electromagnetic, heat flow, mantle xenolith composition) in either its forward or inverse version requires solving a number of equations describing the various physical (e.g., heat transport, Maxwell's equations, or seismic wave propagation) and chemical (thermodynamic mineral phase equilibria) processes that link the thermochemical conditions within the Earth to those geophysical–petrological observables (Dobson and Brodholt 2000; Xu

et al. 2000; Shapiro and Ritzwoller 2004; Khan et al. 2006; Afonso et al. 2008; Verhoeven et al. 2009; Fullea et al. 2009; Zunino et al. 2016). An essential ingredient of the integrated approach is to determine, within a self-consistent thermodynamic framework, key physical parameters in the mantle (e.g., density, resistivity, elastic moduli) as a function of the pressure, temperature, and bulk mineralogical composition (e.g., Connolly 2005; Khan et al. 2007; Afonso et al. 2008; Fullea et al., 2011; Khan 2016, Kuskov et al. 2014). Modelling several data sets simultaneously reduces significantly the uncertainties related to the modelling of these data sets separately or in pairs. This section gives an overview of the main ingredients in the integrated geophysical–petrological approach focused on the lithosphere, including the basic definitions (3.1 The lithosphere–asthenosphere boundary, 3.2 The geotherm), the petrological and mineralogical components (3.3 Thermodynamic framework, 3.4. Mantle bulk electrical conductivity), and the observations (3.5 Forward modelling: geophysical observables). The overview is illustrated by an example from Vozar et al. (2014), where the authors presented a 1D joint forward modelling of long-period surface wave phase velocities, MT responses, and surface topography in central Tibet (Qiangtang and Lhasa terranes).

3.1 The Lithosphere–Asthenosphere Boundary

The lithosphere–asthenosphere boundary (LAB) is one of the fundamental discontinuities within the upper mantle and a commonly used term in integrated modelling. It has been characterized according to different geophysical and geochemical parameters: seismic velocities, seismic and electrical anisotropy, temperature, composition, electrical resistivity (e.g., Eaton et al. 2009; Muller et al. 2009; Jones et al. 2010; Yuan and Romanowicz 2010; Fullea et al., 2011, 2012; Pommier et al. 2015). The LAB divides the outermost, cold, relatively rigid layer of the Earth (lithosphere) from the warmer and rheologically weaker sublithospheric or asthenospheric mantle. A number of different reasons have been proposed to explain the weak rheological nature of the asthenosphere, most notably anisotropy, partial melt and/or the presence of relatively small amounts of water (e.g., Anderson and Sammis 1970; Hirth and Kohlstedt 1996; Kawakatsu et al. 2009; Poe et al. 2010; Karato 2012; Schmerr 2012; Pommier et al. 2015; Laumonier et al. 2017). Here we define the LAB as both a thermal (see Sect. 3.2) and a chemical boundary (see Sect. 3.3).

3.2 The Geotherm

The lithospheric geotherm is computed under the assumption of steady-state heat conduction transfer in the crust and lithospheric mantle for a set of fixed boundary conditions, considering a P–T-dependent thermal conductivity (Afonso et al. 2008; Fullea et al. 2009). In particular, the base of the lithosphere is defined here by the 1300 C isotherm, which is the bottom fixed-temperature boundary condition for the conduction equation. In the convecting sublithospheric mantle, the geotherm is given by an adiabatic temperature gradient (generally assumed to be in the range 0.35–0.6 C/km). Here we assume a mantle adiabat characterized by a potential temperature of 1345 C (e.g., Herzberg et al. 2007). Between the lithosphere and sublithospheric mantle, we parameterize a "transition" region (a buffer or boundary layer) of variable thickness and characterized by super adiabatic gradient (i.e. heat transfer is controlled by both conduction and convection mechanisms, see Fullea et al. (2009) for details). At the 410-km discontinuity (olivine to wadsleyite transition), maximum lateral temperature variations are $\sim$ 120 °C, according to seismic

observations (e.g., Chambers et al. 2005, and references therein, Khan et al. 2013; Kuskov et al. 2014).

3.3 Thermodynamic Framework

Stable mineral assemblages in the mantle can be determined using a Gibbs free energy minimization approach as described by Connolly (2005) and Connolly (2009). The compositional space is usually defined within the major oxide system NCFMAS (Na_2O–CaO–FeO–MgO–Al_2O_3–SiO_2). The NCFMAS compositional space can be treated as six independent variables (i.e. the weight amount of each of the major oxides linked by the restriction that the sum of all of them has to be 100%). The NCFMAS system accounts for > 98 wt.% of the Earth's crust and mantle, and therefore, it is considered to be an excellent starting basis for modelling mineral phase assemblages in the Earth. Based on empirical relationships from global xenolith and peridotite massif databases, the number of independent oxides can be reduced to one or two (usually Al_2O_3 and FeO, see, for example, Afonso et al. 2013a). Other authors parameterize the compositional space in terms of a one-parameter basalt–harzburgite mixture, either a chemically equilibrated bulk composition (e.g., Khan 2016) or a mechanical mixture of the basaltic and harzburgitic end-members (Xu et al. 2008).

In our case study in Tibet, we follow the compositional parameterization based on the NCFMAS system as in, for example, Fullea et al. (2010), (2014); (2015a, b). We define two chemically distinct mantle domains in our 1D model column: the lithospheric mantle and the sublithospheric mantle. In the sublithospheric mantle, we assume an average and fixed fertile primitive composition (i.e. PUM in Table 4). The bulk composition in the lithospheric mantle is a model parameter. Vozar et al. (2014) considered different possible

Table 4 Bulk mantle compositions in Vozar et al. (2014)

	Mongolia: Av. Gnt peridotite (wt.%)[a]	Lhasa 1: dry Fe-rich harz. (ol/opx) (wt.%)[b]	Lhasa 2: dry Fe-rich harz. (ol/opx/cpx) (wt.%)[b]	Lhasa 3: wet Fe-rich harz. (ol/opx/cpx/sp/phl) (wt.%)[b]	PUM M&S95 (wt.%)[c]
SiO_2	44.59	43.44	43.2	42	45
TiO_2	0.14	–	–	–	0.201
Al_2O_3	3.48	0.44	0.96	2.24	4.45
Cr_2O_3	0.4	–	–	–	0.384
FeO	8.25	10.6	10.3	10.37	8.05
MnO	0.14	–	–	–	0.135
MgO	39.56	44.42	44.6	43.2	37.8
CaO	2.85	0.36	0.82	0.61	3.55
Na_2O	0.31	0.02	0.04	0.04	0.36
NiO	0.26	–	–	–	–
Total	99.98	99.28	99.92	98.5	99.93
Mg#	89.7	87.96	88.2	88.14	89.3

[a] Average gnt peridotite from central Mongolia–Baikal from Ionov (2002 and references therein)

[b] Harzburgite averages in Sailipu (West Lhasa) from Liu et al. (2011)

[c] PUM stands for primitive upper mantle, M&S95 refers to McDonough and Sun (1995)

compositions based on xenolith data from western Lhasa (Liu et al. 2011) as well as on average garnet peridotite compositions from Asian mantle xenolith suites (Ionov 2002; Barry et al. 2003) (Table 4).

To solve for the equilibrium mineralogy, different thermodynamically self-consistent databases are available (e.g., Stixrude and Lithgow-Bertelloni 2005, 2011; Ricard et al. 2005; Matas et al. 2007; Khan et al. 2006; Piazzoni et al. 2007). The density and seismic velocities in the mantle can be derived from the elastic moduli and density of each of the stable end-member minerals (e.g., Connolly and Kerrick 2002; Afonso et al. (2008). Anelasticity effects in observed seismic velocities are of primary importance particularly at high temperatures (e.g., Karato and Wu 1993; Sobolev et al. 1996; Goes et al. 2000; Cammarano et al. 2003; Afonso et al. 2010). Anelasticity is here treated as a posteriori pressure–temperature-dependent correction to the anharmonic velocities computed from thermodynamics (e.g., Afonso et al. 2005; Fullea et al. 2012; Karato and Wu 1993; Minster and Anderson 1981). The applied anelastic correction to high-frequency anharmonic velocities is based on the expressions (e.g., Karato and Wu 1993; Minster and Anderson 1981):

$$\begin{aligned} V_{\mathrm{P}} &= V_{\mathrm{P0}}\left(1-\left(\frac{2}{9}\right)\cot\left(\frac{\pi\alpha}{2}\right)Q_{\mathrm{S}}^{-1}\right) \\ V_{\mathrm{S}} &= V_{\mathrm{S0}}\left(1-\left(\frac{1}{2}\right)\cot\left(\frac{\pi\alpha}{2}\right)Q_{\mathrm{S}}^{-1}\right) \\ Q_{\mathrm{S}}^{-1} &= A\left[\frac{T_0}{d}\exp\left(\frac{-(E+PV^*)}{RT}\right)\right]^{\alpha} \end{aligned} \tag{12}$$

where $Q_{\mathrm{P}} = (9/4)\, Q_{\mathrm{S}}$ is assumed (this is equivalent to assuming an infinite quality factor for the bulk modulus, i.e. $Q_{\mathrm{K}} - 1 \sim 0$). V_{P0} and V_{S0} are the unrelaxed anharmonic velocities at a given temperature (T) and pressure (P) for a given bulk composition, $A = 750$ μm αs-α, $\alpha = 0.26$, $E = 424$ kJ/mol, R is the universal gas constant, d is the grain size, V^* the activation volume, and T_0 the reference oscillation period (Faul and Jackson 2005; Jackson et al. 2002). For further discussion on the effects of other parameters (i.e. grain size, activation volume) on the anelasticity correction, the interested reader is referred to laboratory (e.g., Faul and Jackson 2005; Jackson and Faul 2010) and modelling (Fullea et al. 2012) studies. In our case study in Tibet, we use the same attenuation parameters (d, V^*, and T_0) as in Fullea et al. (2012).

As in the case of the electrical conductivity, melt has a significant impact in both the seismic velocities and the attenuation. Recent experimental studies suggest a decrease in the Vs and Q_{S} values of up to 50% and an order of magnitude, respectively, for a melt fraction of 4% (Chantel et al. 2016).

Uncertainties associated with the thermodynamic modelling (e.g., identity of the stable minerals, the compositions of the minerals, and the elastic properties of the minerals) are difficult to assess due to the nonlinearity of the associated free energy minimization problem and autocorrelations among the various thermodynamic parameters. Estimated values in the elastic properties of minerals yield uncertainties of 1–3, 2–4 and 0.5–1%, in Vp, Vs, and mantle density, respectively (e.g., Kuskov and Fabrichnaya 1994; Connolly and Kerrick 2002; Cammarano et al. 2003; Kennett and Jackson 2009). A recent work by Connolly and Khan (2016) has estimated uncertainties in the phase equilibrium. One of their main conclusions is that mineralogical uncertainties in Vp (3–4%) and density (2–3%) are similar to those associated with mineral composition and elastic properties, being in addition more important in the upper than in the lower mantle. However, for Vs the total

uncertainty is comparatively higher (5%), approximately depth independent, and dominated by the elastic properties-related component (Connolly and Khan 2016).

3.4 Mantle Bulk Electrical Conductivity

The bulk conductivity of a mantle rock can be computed knowing its mineral modal distribution and the conductivity of the individual mineral phases (see Sect. 2.2). There are different mixing theories described in the literature to obtain the conductivity of a mineral assemblage based on its geometrical distribution (Maxwell–Garnett 1904; Hashin and Shtrikman 1963; Schulgasser 1976, 1977; Berryman 1995). These mixing theories have been employed by different authors in real case EM studies (e.g., Xu et al. 2000, Ledo and Jones 2005; Jones et al. 2009a). Two-phase systems describing conductive and non-conductive regimes have been generally applied for simplified geometrical representations (e.g., Spangenberg 1998; Kozlovskaya and Hjelt 2000). However, these approaches are less relevant for the Earth because the crucial information about the texture of rocks is in general missing and only poorly sampled in xenoliths and other exposed mantle rocks. Therefore, the bulk conductivity of mantle rocks is better described by means of averaging schemes involving no assumptions in terms of the phase geometry. Maxwell-Garnett (1904) developed the concept of the most extreme bounds that can possibly be obtained for a physically meaningful mixture without any textural assumptions ("extremal bounds"). The Hashin–Shtrikman (HS) extremal bounds (Hashin and Shtrikman 1963) are the narrowest possible limits for a two-phase composite without assuming any information about the texture/geometry of the phases. The generalization of the HS bounds for the conductivity of an N-phase material is given by (Berryman 1995):

$$\sigma_{\mathrm{HS}}^{-} = \left(\sum_{i=1}^{N} \frac{v_i}{\sigma_i + 2\sigma_{\min}} \right)^{-1} - 2\sigma_{\min} \tag{13}$$

where σ_{HS}^{-} is the lower bound, v_i is the volume fraction, N the number of phases, and $\sigma_{\min}$ is the minimum conductivity of the N individual phases (see Sect. 2.2). In a similar way, the upper bound, σ_{HS}^{+}, in Eq. 13 results from replacing the maximum value, $\sigma_{\max}$, for the minimum one. The minimum bound σ_{HS}^{-} can be thought of as resistive matrix filled with non-interconnected conductive inclusions. σ_{HS}^{+} would be represented by a conductive matrix with non-interconnected resistive inclusions. Another set of bounds widely used to characterize the electrical conductivity of mineral assemblages are the series and parallel solutions (Schulgasser 1976, 1977):

$$\begin{aligned} \sigma_{\mathrm{S}} &= \left(\sum_{i=1}^{N} \frac{v_i}{\sigma_i} \right)^{-1} \\ \sigma_{\mathrm{P}} &= \left(\sum_{i=1}^{N} \sigma_i v_i \right) \end{aligned} \tag{14}$$

where σ_{S} and σ_{P} are the series and parallel solutions, respectively. The series solution represents the minimum bound, whereas the parallel solution is the maximum bound. From a practical point of view, the differences between the series and parallel solutions and the HS bounds are relatively minor (e.g., Fullea et al. 2011) and the geometrical average between the min and max bounds in any of the two cases is a good estimation of the bulk rock conductivity.

3.5 Forward Modelling: Geophysical Observables

Density and pressure are mutually inter-related, and their distribution in depth has to be found following an iterative procedure (see Appendix B in Fullea et al. 2009). Once temperature, density, seismic velocities, and electrical conductivity distributions have been derived in 1D, 2D, or 3D (see Sects. 3.1–3.4 above), a variety of synthetic geophysical observables can be computed: surface heat flow, elevation, gravity field anomalies, and seismic and electromagnetic data sets. These theoretical/predicted values are then compared to measured data in order to validate Earth models either sequentially (i.e. forward modelling) or within an inversion scheme.

In our case study in Tibet, Vozar et al. (2014) modelled the 1D lithospheric mantle structure using surface wave phase dispersion curves, MT responses, and surface topography with additional constraints from mantle xenoliths and surface heat flow. The main model parameters in Vozar et al. (2014) are the Moho and LAB depths, controlling to a large extent the geotherm, and the mantle bulk composition and hydrous state. Other parameters like crustal properties (velocities, resistivity, and thermal parameters) and a radial anisotropy profile were taken from previous studies and kept fixed (see Vozar et al. 2014 and references therein). The surface wave Rayleigh and Love phase velocities in Tibet modelled in Vozar et al. (2014) were measured by Agius and Lebedev (2013) over a period range broad enough to sense the lithosphere (Fig. 8). The MT data modelled in Vozar et al. (2014) come from INDEPTH project line 500 (Fig. 8). From the whole INDEPTH 500 line, a subsection of the MT stations was selected by Vozar et al. (2014) (marked by circles in the north (purple—ii) and south (red—i) in Fig. 8 insert). Based on skin depth and consistency considerations, MT data from the TE mode were selected for integrated 1D modelling in the Lhasa Block and the Qiangtang Terrane. Data from stations within the two groups (i.e. Lhasa and Qiangtang) exhibit significant similarities in their sounding curves (Fig. 9). Synthetic local isostatic topography was estimated integrating the crustal and lithospheric mantle density down to a reference compensation level. According to the isostatic principle, the density-dependent pressure at the so-called compensation level should be constant everywhere, and therefore, it is possible to use a calibrated reference column (usually a mid-oceanic rift, see Afonso et al. 2008 and Fullea et al. 2009 for details) to determine absolute elevation as a measure of lithospheric buoyancy. Although not considered in the Tibet case study, lithospheric flexure effects related to the effective elastic thickness and the wavelengths of the loads can also be included (see Appendix C2 in Fullea et al. 2009),

In the Qiangtang Terrane (Fig. 8), the best-fitting lithospheric model shows a 100-km-thick lithosphere with a relatively fertile and dry lherzolitic composition (Mongolian composition in Table 4) (Fig. 10). This best-fitting model is able to match the observed MT responses and Rayleigh and Love phase velocities, and also the average topography of the area in an isostatic sense (4.8 km). The crust in the best-fitting model is defined by a Moho depth of 66 km in agreement with the existing literature (e.g., Zhao et al. 2001; Kind et al. 2002; Kumar et al. 2006; Li et al. 2006; Yue et al. 2012). For illustrative purposes, Fig. 10 shows the effect on the synthetic geophysical observables of changing in 20 km the thickness of the lithosphere in the best-fitting model. In the southern part of the Lhasa Terrane (Fig. 8), both the crust and the lithosphere are thicker (75 and 180 km, respectively) than in Qiangtang according to modelling of surface wave and elevation data. This lithospheric structure, however, is unable to explain the long-period MT data if the mantle is assumed to be dry; in such a case, the electrical resistivity is too elevated regardless of

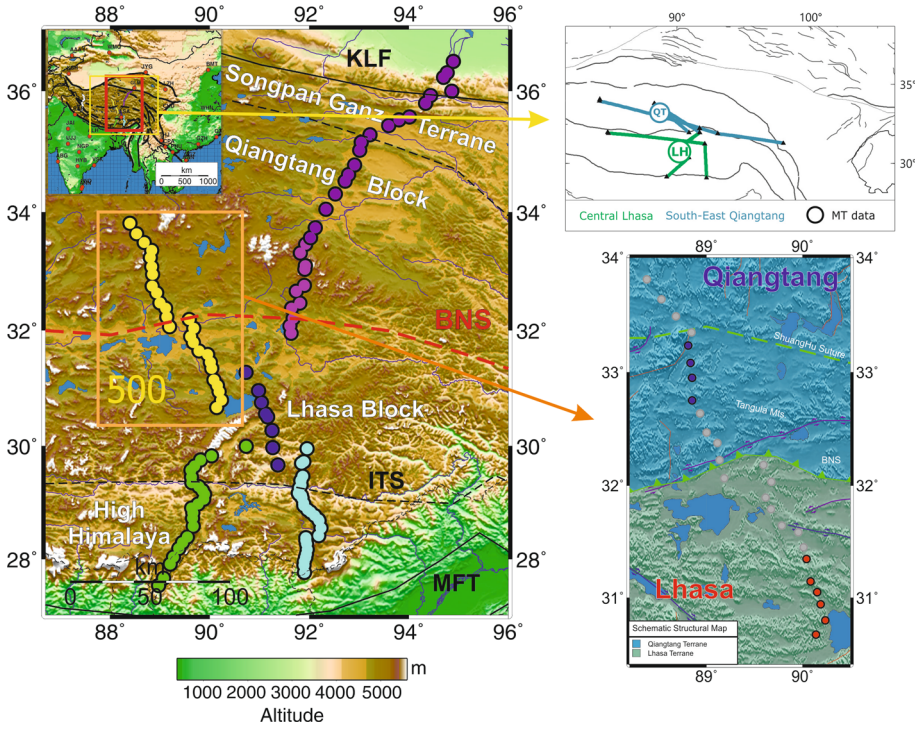

Fig. 8 Maps showing the locations of INDEPTH MT profiles in Tibet (different colours). BNS, Banggong–Nujiang suture; ITS, Indus–Tsangpo suture; MBT, main frontal thrust; KLF, Kunlun fault; SS, Shuanghu suture. (Top right) Map of seismic stations used for surface wave modelling in Vozar et al. (2014). (Bottom right) Zoomed map of line 500 with highlighted sites from the Lhasa and Qiangtang Blocks used for analysis in Vozar et al. (2014)

the assumed lithospheric thickness (i.e. geotherm). There are several factors that can very effectively decrease the electrical resistivity of the mantle (e.g., minor conducting phases, melt, or water, see Sect. 2.2). Vozar et al. (2014) explored the hypothesis of small amounts of water (hundreds of wt ppm) in nominally anhydrous minerals (NAMs). At this scale, water significantly decreases mantle resistivity with a negligible effect in the density and seismic velocities and associated observables. In addition, the presence of hydrous minerals (i.e. phlogopite) observed in some of the Fe-rich harzburgites in xenoliths from Sailipu, a Lhasa terrain location west of the study region (Liu et al. 2011, Table 4), further suggests a wet mantle. On those grounds, Vozar et al. (2014) modelled Lhasa mantle with a phlogopite-bearing Fe-rich spinel harzburgite composition based on xenoliths from West Lhasa (Lhasa 3 composition in Table 4). Vozar et al. (2014) considered three olivine proton conduction models to estimate the amount and vertical distribution of water in the Tibetan/Indian mantle: (1) Wang et al. (2006); (2) Yoshino et al. (2009); and (3) Jones et al. (2012). The different olivine proton conduction models considered in Vozar et al. (2014) require bulk water contents ranging from tens to hundreds wt ppm to match the MT data, assuming water partitioning among the different minerals based on laboratory studies (e.g., Kovács et al. 2012, see Table 3). Vertically, the water distribution in the preferred model is constant from the Moho to 160 km, decreasing down to the LAB depth at 180 km (green line in Fig. 11). Alternative water distributions in olivine are shown in Fig. 11. A

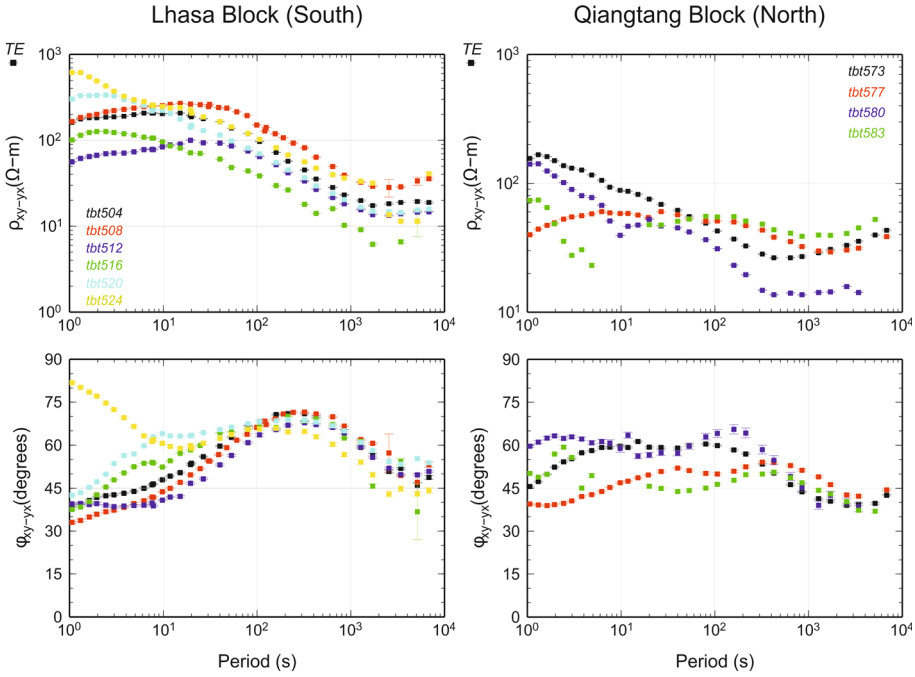

Fig. 9 Apparent resistivities and impedance phases of the TE (transverse electric) magnetotelluric mode decomposed to regional strike direction for selected sites in the Lhasa and Qiangtang Blocks. The data are used in integrated geophysical–petrological study by Vozar et al. (2014)

completely wet mantle (red line in Fig. 11) produces a very conducting mantle unable to match MT data. In contrast, a completely dry (yellow line) or linearly decreasing water content lithospheric model (blue line) is too resistive (Fig. 11). The best-fitting models underneath Lhasa suggest a relatively wet underthrusting Indian lithosphere (depth < 180 km) likely caused by dehydration processes. Vozar et al. (2014) interpreted the thick lithosphere under Lhasa as a result of the underthrusting or low-angle subduction without a significant downwelling of a relatively warm and wet Indian lithosphere beneath Tibet. This process would have triggered metasomatism in a previously depleted Tibetan lithosphere as evidenced by the Fe enrichment and the inferred rehydration.

4 Discussion

As illustrated by the case study in Tibet, integrated geophysical–petrological joint modelling of both seismological and electromagnetic data simultaneously including the constraints offered by topography, mantle xenoliths and surface heat flow has the potential to yield superior inferences than using either of them independently due to their different sensitivities to temperature and composition (i.e. modal mineralogy and water content). The grey areas in the seismic velocity and resistivity profiles in Fig. 10 (bottom panel) represent the uncertainties in the secondary parameters derived from purely seismic and purely MT inversion of the seismic and MT data sets, respectively (see Vozar et al. 2014 and references therein). It is clear that the range of integrated models that match the

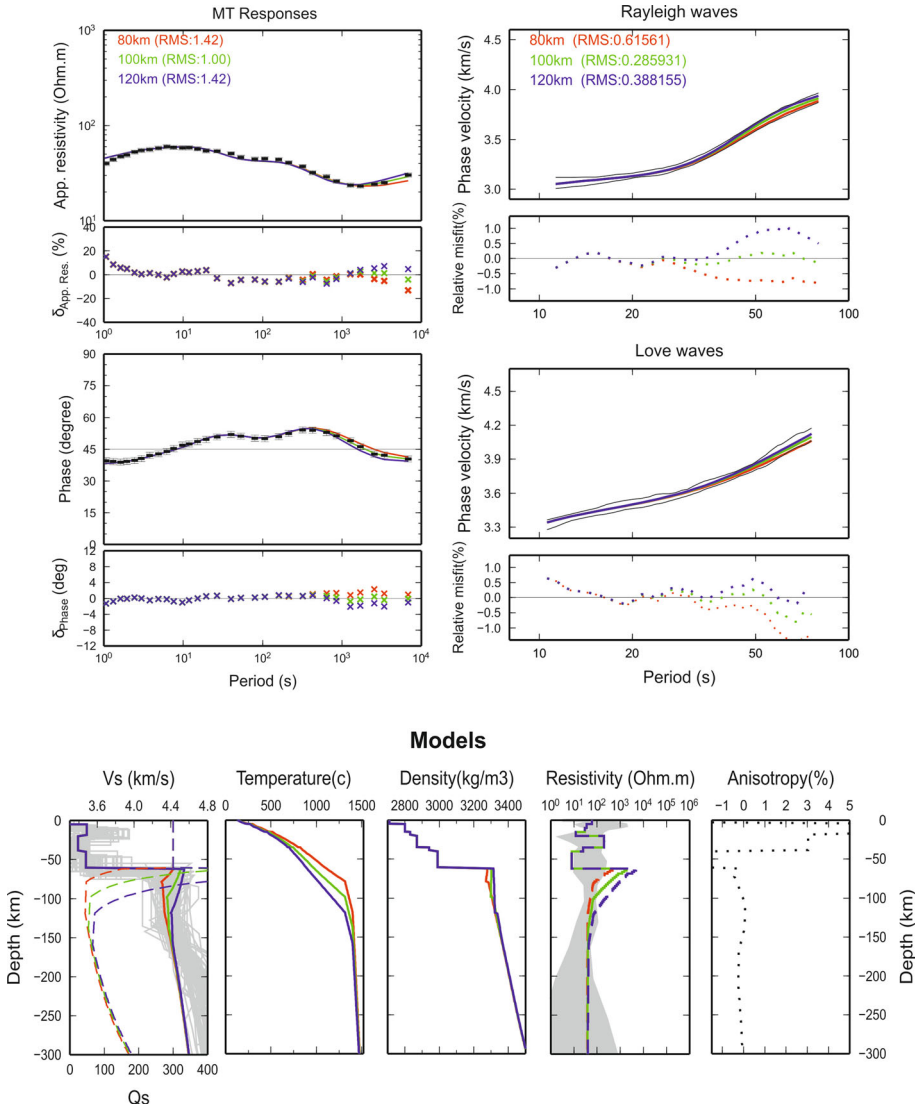

Fig. 10 Integrated geophysical–petrological models of the Qiangtang region for a dry mantle composition (Mongolian Av. Gnt Peridotite, Table 4). (Top) Fits of MT and seismic data for three (red—80 km, green—100 km, and blue—120 km) different thermal lithosphere–asthenosphere boundary (LAB) depths. (Bottom) Corresponding calculated models of *Vs* velocities (dashed lines represent shear wave quality factors *Q*s, grey lines represent all possible models based only on seismic modelling), temperature, density, resistivity (grey area—the range of all resistivity models based only on MT data), and anisotropy. Seismic anisotropy values are fixed based on the best-fitting model from Agius and Lebedev (2013). See the text (Sect. 3) for a description on how temperature, *Vs*, density, and *Q*s values are computed within the integrated approach

constraining data sets within their error bars defines a considerable narrower area in the secondary parameter space (coloured lines in Fig. 10). More importantly, within the integrated modelling approach we are not trying to find a thermochemical model that simultaneously corresponds to some plausible velocity, density, and resistivity model (that

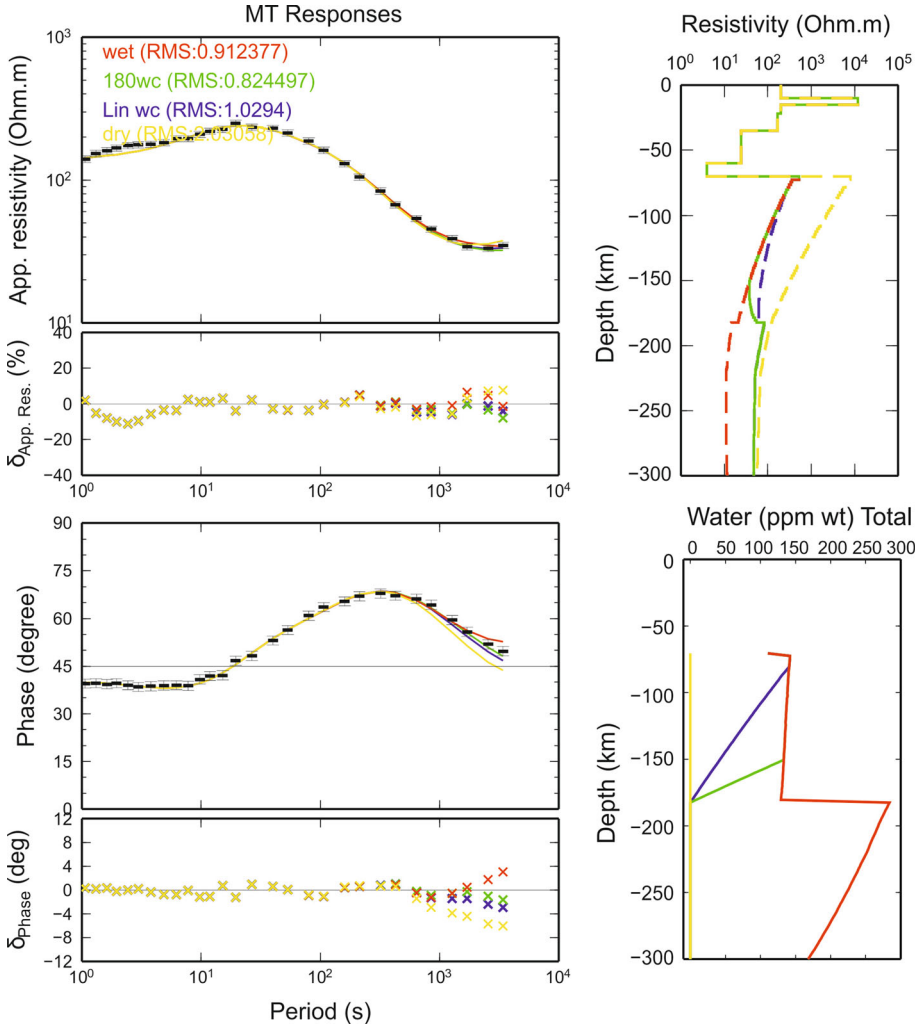

Fig. 11 Integrated geophysical–petrological models in Lhasa for four different bulk water distributions within the mantle: blue—linear decrease from 80 km to LAB depth at 180 km, green—constant down to 160 km and then linear decrease to 180 km, red—full wet mantle, and yellow—dry mantle. Olivine's solubility is modelled according to the work by Zhao et al. (2004) (see Fig. 3 and Sect. 2.2.1 in the main text)

already exhibits a considerable variability, see Fig. 10); instead, we are trying to find temperature and compositional models that can simultaneously explain the input seismic, MT, and elevation data with appropriate assumptions regarding the underlying physical process involved. In this way, we also mitigate to some extent the non-uniqueness of converting point-wise (in this particular 1D example depth-wise) secondary parameter models of velocities, resistivity, or density into temperature and composition (see Sect. 2.3) as often done in the literature (e.g., Cammarano et al. 2003; Simmons et al. 2010; Thiel and Heinson 2013; Ichiki et al. 2015; Cammarano and Guerri 2017).

The study case considered here in Tibet was modelled in 1D. Surface wave dispersion data, either coming from the two-station (e.g., Agius and Lebedev 2013) or the ambient noise technique (e.g., Yang et al. 2008), can adequately be modelled in 1D in as much as the effects of azimuthal anisotropy are accounted for (e.g., Adam and Lebedev 2012). In the case of MT data, the situation is considerably more complex. The dimensionality of MT data can be due to 2D–3D electrical structures in the vicinity of the measuring point but also can be related to intrinsic 1D microscopic anisotropy, the difference between the two scenarios being subtle in general (e.g., Wannamaker 2005; Adetunji et al. 2015; Martí 2014). Therefore, in order to apply the 1D integrated methodology presented here a careful analysis of the MT data (e.g., dimensionality, regional strike, distortion) should be carried out first to ensure the suitability of the data for 1D modelling. For example, in the study case taken here, after the dimensionality, regional strike, decomposition, and consistency analyses were conducted, TE mode was deemed the most suitable data to represent the average 1D lithospheric structure in the area. This, however, should not be taken as a general rule: TM mode, an invariant or even synthetic responses from a 3D inversion model, could be more appropriate given the case. Each scenario should be assessed distinctively based on the context.

The method presented here is focused on the mantle structure. Under the prevalent conditions in the mantle, the assumption of thermodynamic equilibrium is valid, and therefore, secondary parameters in the Earth (resistivity, density, seismic velocities) can be self-consistently determined using geophysical and petrological modelling tools (e.g., LitMod, Perple_X). In contrast to the mantle, where thermodynamic equilibrium is prevalent, vast portions of the continental crust are thermodynamically metastable. This is because equilibration processes are essentially temperature-activated and the temperature in the crust is usually too low (< 500 C) to trigger them. Consequently, the mineralogical assemblage of crustal rocks is mostly decoupled from the in situ pressure and temperature conditions, reflecting instead the conditions present at the moment of rock formation. In addition to this complication, the variety of existing mineral phases in the crust is considerably wider than that in the mantle. There are comparatively fewer electrical conductivity experiments conducted for crustal minerals, and it is well known that factors other than temperature and pressure can greatly affect the conductivity of crustal rocks (e.g., porosity, fluids). Considering all these restrictive factors together, we can conclude that the application of the integrated method to investigate the crust using EM data is not yet viable.

One of the major restrictions of integrated forward modelling is the size and complexity of parameter space, and the trade-offs between the different variables. In addition, uncertainties and the non-uniqueness of the derived forward models are rather difficult to quantify. Probabilistic (Bayesian) inversions are a powerful option to circumvent all these difficulties, while allowing for an adequate treatment of the intrinsic uncertainties associated with both input data and chemical-physical theories and processes involved (e.g., Khan et al. 2006, 2007; Afonso et al. 2013a, b). Bayesian inversions characterize the parameter space in terms of the so-called posterior probability density function (PDF) which contains all current information about the problem considered and represents an objective measure of our best state of knowledge on the problem. The posterior PDF contains a term describing all a priori information in the data and parameter space and the so-called likelihood function which measures how well a particular model explains the observations. The likelihood function contains a term describing the correlations and uncertainties of any physical–chemical theory connecting model parameters and predicted observations (covariance matrix). The Likelihood function can be determined in a

straightforward manner (e.g., Khan et al. 2006), but the choice of the prior PDF on the model parameters is not trivial and often is controversial. The main information the prior PDF on the parameters should contain is everything known about the problem that is independent of the observed data, and how certain we are about this knowledge. For an extensive description about how to describe and characterize the prior PDF on the thermochemical parameters, the reader is referred to Afonso et al. (2013a).

5 Concluding Remarks

This paper is intended to review the joint modelling and interpretation of electromagnetic data and other geophysical and petrological observables. The necessity of consistently combining different observations and techniques has been often highlighted in the literature in the past. However, the materialization of such joint efforts perhaps has been less generous in terms of dedicated studies, and especially so in the EM research field. This tendency seems to be fortunately overcome, with many relevant studies being published in the last few years from both the experimental and the geophysical sides. Integrated geophysical–petrological joint modelling of electromagnetic and other data sets has the potential to yield superior inferences than using either data set independently. In particular, EM techniques are very sensitive to minor constituents (e.g., melt and water) and textural characteristics of rocks (anisotropy). Precise knowledge of those minor rock constituents along with the fabric anisotropy is crucial to characterize rock rheology and deformation: that is, the geodynamic evolution of the Earth. One of the main challenges in interpreting EM data is to connect electrical conductivity models with the thermochemical conditions within the Earth or, in other words, to disentangle the in situ thermal, chemical, and textural components of the Earth's conductivity distribution, which are linked in a highly nonlinear manner. In that sense, integrated geophysical–petrological modelling of EM and other data sets offers the advantage of naturally exploiting the complementary sensitivities of the various observations within a consistent framework reducing therefore the uncertainties. Seismic measurements are mostly sensitive to temperature, and hence, an integrated modelling of them along with EM data within a common thermodynamic setting allows striping off the thermal component in the electrical conductivity field. The former makes possible focusing on the distribution of minor rock components that are, for the most part, invisible to other geophysical observations (e.g., seismological, gravity).

The integrated modelling example presented here in Tibet corresponds to a 1D approximation to the Earth. To the best of my knowledge, integrated geophysical–petrological studies (either forward modelling or inversion) including EM data have only been carried out in the 1D approximation so far (Fullea et al. 2011; Khan and Shankland 2012; Koyama et al. 2014; Vozar et al. 2014). This has the advantage of simplicity but of course the limitation of artificially reducing the complexity of the real Earth. An extension of the integrated approach to 2D or 3D would be desirable and in some cases even necessary depending on the complexity of the EM data considered. In its forward modelling version, this is at hand as there are several efficient MT solvers in 2D and 3D that could be coupled with integrated models. The MT solvers would calculate the synthetic responses associated with volumetric resistivity distributions self-consistently computed based on thermochemical structure derived from other geophysical observations. This would be a natural step forward in our interpretation of large MT arrays, particularly useful in cases where collocated seismic data are available on top of other public global data sets like gravity or

magnetics (e.g., USArray, SinoProbe, SAMTEX). The 2D–3D move towards integrated inversion would be more challenging, particularly in 3D, due to the considerable computational time required by the state-of-the-art forward solvers; in spite of this, alternative strategies like dimensionally adaptive grids could be explored to alleviate the computational cost (e.g., Ledo et al. 2002; Alvarez-Aramberri and Pardo 2017).

Integrated modelling relies heavily on the constraints offered by thermodynamic databases and mineral physics experiments which are, to some extent, subjected to uncertainties, discrepancies and problems related to their extrapolation to the Earth's temperature, hydrous and pressure conditions, particularly in the case of electrical conductivity. This fact reflects the geophysical community's urgent need for further experiments that can overcome or mitigate such limitations in the future. At the same time, integrated geophysical studies host the potential to explore and test at large scales, and even globally, measurements or hypotheses that the experimental community can only probe at the microscopic scale and under rather restrictive and controlled thermochemical conditions. At regional and local scales, the benefits of integrative studies combining EM with other disciplines have proved to be considerable. At global scales, the advent of high-precision and high-resolution magnetic field satellite measurements with uniform global coverage, along with long-term geomagnetic observatory data, is enabling the development of a new generation of global electrical conductivity models of the crust and mantle. Yet those conductivity models still need to be appropriately and consistently integrated with other global observations (e.g., seismic tomography, satellite gravity data, deformation) to produce a coherent structural and rheological image of the Earth.

Acknowledgements The author is thankful to Ian Ferguson and the other organizers of the 23rd Electromagnetic Induction Workshop in Chiang Mai for inviting this review paper. Topical editor Ute Weckmann, Amir Khan, and one anonymous reviewer helped to improve this paper with their constructive criticism. J. Fullea has received funding from the People Programme (Marie Curie Actions) of the European Union's H2020-MSCA-IF-2014 programme (REA Grant agreement no 657357) and Science Foundation Ireland grant 16/ERCD/4303 that supported the work presented here. Finally, I want to thank *Olivia* for giving me the strength and inspiration to carry on in the most difficult circumstances.

References

Adam JMC, Lebedev S (2012) Azimuthal anisotropy beneath southern Africa from very broad-band surface-wave dispersion measurements. Geophys J Int 191(1):155–174

Adetunji AQ, Ferguson IJ, Jones AG (2015) Reexamination of magnetotelluric responses and electrical anisotropy of the lithospheric mantle in the Grenville Province, Canada. J Geophys Res Solid Earth 120(3):1890–1908

Afonso JC, Ranalli G, Fernàndez M (2005) Thermal expansivity and elastic properties of the lithospheric mantle: results from mineral physics of composites. Phys Earth Planet Inter 149:279–306

Afonso JC, Fernàndez M, Ranalli G, Griffin WL, Connolly JAD (2008) Integrated geophysical–petrological modeling of the lithosphere and sublithospheric upper mantle: methodology and applications. Geochem Geophys Geosyst 9:Q05008. doi:10.1029/02007GC001834

Afonso JC, Ranalli G, Fernàndez M, Griffin WL, O'Reilly SY, Faul U (2010) On the Vp/Vs–Mg# correlation in mantle peridotites: implications for the identification of thermal and compositional anomalies in the upper mantle. Earth Planet Sci Lett 289:606–618

Afonso J, Fullea J, Griffin W, Yang Y, Jones A, Connolly JD, O'Reilly S (2013a) 3-D multiobservable probabilistic inversion for the compositional and thermal structure of the lithosphere and upper mantle. I: a priori petrological information and geophysical observables. J Geophys Res Solid Earth 118:2586–2617

Afonso JC, Fullea J, Yang Y, Connolly J, Jones A (2013b) 3-D multi-observable probabilistic inversion for the compositional and thermal structure of the lithosphere and upper mantle. II: general methodology and resolution analysis. J Geophys Res Solid Earth 118:1650–1676
Agius MR, Lebedev S (2013) Tibetan and Indian lithospheres in the upper mantle beneath tibet: evidence from broadband surface-wave dispersion. Geochem Geophys Geosyst 14:4260–4281
Alvarez-Aramberri J, Pardo D (2017) Dimensionally adaptive hp-finite element simulation and inversion of 2D magnetotelluric measurements. J Comput Sci 18:95–105
Anderson DL (2000) The thermal state of the upper mantle; no role for mantle plumes. Geophys Res Lett 27(22):3623–3626
Anderson DL, Sammis C (1970) Partial melting in the upper mantle. Phys Earth Planet Inter 3:41–50
Ardia P, Hirschmann M, Withers A, Tenner T (2012) H_2O storage capacity of olivine at 5–8 GPa and consequences for dehydration partial melting of the upper mantle. Earth Planet Sci Lett 345:104–116
Asimow PD, Dixon JE, Langmuir CH (2004) A hydrous melting and fractionation model for mid-ocean ridge basalts: application to the Mid-Atlantic Ridge near the Azores. Geochem Geophys Geosyst 5:Q01E16. doi:10.1029/2003GC000568
Aubaud C, Hauri EH, Hirschmann MM (2004) Hydrogen partition coefficients between nominally anhydrous minerals and basaltic melts. Geophys Res Lett 31:L20611. doi:10.1029/2004GL021341
Baba K, Utada H, Goto T-N, Kasaya T, Shimizu H, Tada N (2010) Electrical conductivity imaging of the Philippine Sea upper mantle using seafloor magnetotelluric data. Phys Earth Planet Inter 183:44–62
Bai Q, Kohlstedt D (1993) Effects of chemical environment on the solubility and incorporation mechanism for hydrogen in olivine. Phys Chem Miner 19:460–471
Bali E, Bolfan-Casanova N, Koga K (2008) Pressure and temperature dependence of H solubility in forsterite: an implication to water activity in the Earth interior. Earth Planet Sci Lett 268:354–363
Baptiste V, Tommasi A, Demouchy S (2012) Deformation and hydration of the lithospheric mantle beneath the Kaapvaal craton, South Africa. Lithos 149:31–50
Barry TL, Saunders AD, Kempton PD, Windley BF, Pringle MS, Dorjnamjaa D, Saandar S (2003) Petrogenesis of Cenozoic basalts from Mongolia: evidence for the role of asthenospheric versus metasomatized lithospheric mantle sources. J Pet 44(1):55–91
Bell DR, Rossman GR (1992) The distribution of hydroxyl in garnets from the subcontinental mantle of southern Africa. Contrib Mineral Petrol 111:161–178
Bell DR, Ihinger PD, Rossman GR (1995) Quantitative analysis of trace OH in garnet and pyroxenes. Am Mineral 80:465–474
Bell DR, Rossman GR, Maldener J, Endisch D, Rauch F (2003) Hydroxide in olivine: a quantitative determination of the absolute amount and calibration of the IR spectrum. J Geophys Res 108(B2):2105. doi:10.1029/2001JB000679
Bell DR, Rossman GR, Moore RO (2004) Abundance and partitioning of OH in a high-pressure magmatic system: megacrysts from the Monastery kimberlite, South Africa. J Petrol 45:1539–1564
Berryman JG (1995) Mixture theories for rock properties. In: Ahrens TJ (ed) American geophysical union handbook of physical constants. AGU, New York, pp 205–228
Cammarano F, Guerri M (2017) Global thermal models of the lithosphere. Geophys J Int 210(1):56–72
Cammarano F, Goes S, Vacher P, Giardini D (2003) Inferring upper-mantle temperatures from seismic velocities. Phys Earth Planet Inter 138:197–222
Caricchi L, Gaillard F, Mecklenburgh J, Le Trong E (2011) Experimental determination of electrical conductivity during deformation of melt-bearing olivine aggregates: implications for electrical anisotropy in the oceanic low velocity zone. Earth Planet Sci Lett 302(1):81–94
Chakraborty S (2010) Diffusion coefficients in olivine, wadsleyite and ringwoodite. Rev Mineral Geochem 72:603–639
Chambers K, Woodhouse J, Deuss A (2005) Topography of the 410-km discontinuity from PP and SS precursors. Earth Planet Sci Lett 235:610–622
Chantel J, Manthilake G, Andrault D, Novella D, Yu T, Wang Y (2016) Experimental evidence supports mantle partial melting in the asthenosphere. Sci Adv 2(5):e1600246
Connolly JAD (2005) Computation of phase equilibria by linear programming: a tool for geodynamic modeling and its application to subduction zone decarbonation. Earth Planet Sci Lett 236:524–541
Connolly JAD (2009) The geodynamic equation of state: what and how. Geochem Geophys Geosyst 10:Q10014. doi:10.1029/2009GC002540
Connolly J, Kerrick D (2002) Metamorphic controls on seismic velocity of subducted oceanic crust at 100–250 km depth. Earth Planet Sci Lett 204:61–74
Connolly JAD, Khan A (2016) Uncertainty of mantle geophysical properties computed from phase equilibrium models. Geophys Res Lett 43(10):5026–5034
Constable S (2006) SEO3: a new model of olivine electrical conductivity. Geophys J Int 166:435–437

Dai L, Karato S-I (2009a) Electrical conductivity of orthopyroxene: implications for the water content of the asthenosphere. Proc Jpn Acad Ser B 85:466–475
Dai L, Karato S-I (2009b) Electrical conductivity of pyrope-rich garnet at high temperature and high pressure. Phys Earth Planet Inter 176:83–88
Dai L, Karato S-I (2014a) The effect of pressure on the electrical conductivity of olivine under the hydrogen-rich conditions. Phys Earth Planet Inter 232:51–56
Dai L, Karato S-I (2014b) High and highly anisotropic electrical conductivity of the asthenosphere due to hydrogen diffusion in olivine. Earth Planet Sci Lett 408:79–86
Dai L, Li H, Liu C, Su G, Shan S (2006) Experimental measurement of the electrical conductivity of pyroxenite at high temperature and high pressure under different oxygen fugacities. High Press Res Int J 26:193–202
Dai L, Li H, Hu H, Shan S, Jiang J, Hui K (2012) The effect of chemical composition and oxygen fugacity on the electrical conductivity of dry and hydrous garnet at high temperatures and pressures. Contrib Mineral Petrol 163:689–700
Dai L, Li H, Hu H, Jiang J, Hui K, Shan S (2013) Electrical conductivity of Alm 82 Py 15 Grs 3 almandine-rich garnet determined by impedance spectroscopy at high temperatures and high pressures. Tectonophysics 608:1086–1093
Demouchy S (2010) Diffusion of hydrogen in olivine grain boundaries and implications for the survival of water-rich zones in the Earth's mantle. Earth Planet Sci Lett 295:305–313
Demouchy S, Bolfan-Casanova N (2016) Distribution and transport of hydrogen in the lithospheric mantle: a review. Lithos 240:402–425
Demouchy S, Mackwell S (2006) Mechanisms of hydrogen incorporation and diffusion in iron-bearing olivine. Phys Chem Miner 33:347–355
Demouchy S, Jacobsen SD, Gaillard F, Stern CR (2006) Rapid magma ascent recorded by water diffusion profiles in mantle olivine. Geology 34:429–432
Didana YL, Thiel S, Heinson G (2014) Magnetotelluric imaging of upper crustal partial melt at Tendaho graben in Afar, Ethiopia. Geophys Res Lett 41:3089–3095
Dobson DP, Brodholt JP (2000) The electrical conductivity and thermal profile of the Earth's mid-mantle. Geophys Res Lett 27(15):2325–2328
Doucet LS, Peslier AH, Ionov DA, Brandon AD, Golovin AV, Goncharov AG, Ashchepkov IV (2014) High water contents in the Siberian cratonic mantle linked to metasomatism: an FTIR study of Udachnaya peridotite xenoliths. Geochim Cosmochim Acta 137:159–187
Du Frane WL, Roberts JJ, Toffelmier DA, Tyburczy JA (2005) Anisotropy of electrical conductivity in dry olivine. Geophys Res Lett 32(24). doi:10.1029/2005GL023879
Duba A (1976) Are laboratory electrical conductivity data relevant to the Earth. Acta Geodaet Geophys Montanist Acad Sci Hung 11:485–496
Eaton DW, Darbyshire F, Evans RL, Grütter H, Jones AG, Yuan X (2009) The elusive lithosphere-asthenosphere boundary (LAB) beneath cratons. Lithos 109:1–22
Fainberg E, Kuvshinov A, Singer BS (1990) Electromagnetic induction in a spherical Earth with non-uniform oceans and continents in electric contact with the underlying medium—II. Bimodal global geomagnetic sounding of the lithosphere. Geophys J Int 102:283–286
Farla R, Peach C, ten Grotenhuis S (2010) Electrical conductivity of synthetic iron-bearing olivine. Phys Chem Miner 37:167–178
Faul UH, Jackson I (2005) The seismological signature of temperature and grain size variations in the upper mantle. Earth Planet Sci Lett 234:119–134
Ferot A, Bolfan-Casanova N (2012) Water storage capacity in olivine and pyroxene to 14 GPa: implications for the water content of the Earth's upper mantle and nature of seismic discontinuities. Earth Planet Sci Lett 349:218–230
Fujii I, Schultz A (2002) The 3D electromagnetic response of the Earth to ring current and auroral oval excitation. Geophys J Int 151:689–709
Fullea J, Afonso JC, Connolly JAD, Fernàndez M, García-Castellanos D, Zeyen H (2009) LitMod3D: an interactive 3-D software to model the thermal, compositional, density, seismological, and rheological structure of the lithosphere and sublithospheric upper mantle. Geochem Geophys Geosyst 10:Q08019
Fullea J, Fernàndez M, Afonso JC, Vergés J, Zeyen H (2010) The structure and evolution of the lithosphere–asthenosphere boundary beneath the Atlantic–Mediterranean Transition Region. Lithos 120:74–95
Fullea J, Muller MR, Jones AG (2011) Electrical conductivity of continental lithospheric mantle from integrated geophysical and petrological modeling: application to the Kaapvaal Craton and Rehoboth Terrane, Southern Africa. J Geophys Res 116:B10202. doi:10.1029/2011JB008544

Fullea J, Lebedev S, Agius MR, Jones AG, Afonso JC (2012) Lithospheric structure in the Baikal–central Mongolia region from integrated geophysical-petrological inversion of surface-wave data and topographic elevation. Geochem Geophys Geosyst 13:Q0AK09. doi:10.1029/2012GC004138

Fullea J, Muller M, Jones A, Afonso J (2014) The lithosphere–asthenosphere system beneath Ireland from integrated geophysical–petrological modeling II: 3D thermal and compositional structure. Lithos 189:49–64

Fullea J, Camacho A, Negredo A, Fernández J (2015a) The canary islands hot spot: new insights from 3D coupled geophysical-petrological modelling of the lithosphere and uppermost mantle. Earth Planet Sci Lett 409:71–88

Fullea J, Rodriguez J, Charco M, Negredo A, Martinec Z, Villaseñor A (2015b) Perturbing effects of sub-lithospheric mass anomalies in GOCE gravity gradient and other potential field data modelling: application to the Atlantic-Mediterranean transition zone. Int J Appl Earth Obs Geoinform, Special volume: GOCE 35:54–69

Gaillard F (2004) Laboratory measurements of electrical conductivity of hydrous and dry silicic melts under pressure. Earth Planet Sci Lett 218:215–228

Gaillard F, Malki M, Iacono-Marziano G, Pichavant M, Scaillet B (2008) Carbonatite melts and electrical conductivity in the asthenosphere. Science 322:1363–1365

Gardés E, Gaillard F, Tarits P (2014) Toward a unified hydrous olivine electrical conductivity law. Geochem Geophys Geosyst 15:4984–5000

Gatzemeier A, Tommasi A (2006) Flow and electrical anisotropy in the upper mantle: finite-element models constraints on the effects of olivine crystal preferred orientation and microstructure. Phys Earth Planet Inter 158:92–106

Gavrilenko P (2008) Water solubility in diopside. Ph.D thesis, Bayerisches Geoinstitut, Universität Bayreuth, Bayreuth, Germany

Glover PW (2010) A generalized Archie's law for n phases. Geophysics 75:E247–E265

Goes S, Govers R, Vacher P (2000) Shallow mantle temperatures under Europe from P and S wave tomography. J Geophys Res Solid Earth 105:11153–11169

Grant K, Ingrin J, Lorand J, Dumas P (2007) Water partitioning between mantle minerals from peridotite xenoliths. Contrib Mineral Petrol 154:15–34

Grayver AV, Schnepf NR, Kuvshinov AV, Sabaka TJ, Manoj C, Olsen N (2016) Satellite tidal magnetic signals constrain oceanic lithosphere-asthenosphere boundary. Sci Adv 2(9):e1600798

Hammouda T, Laporte D (2000) Ultrafast mantle impregnation by carbonatite melts. Geology 28:283–285

Hashin Z, Shtrikman S (1963) A variational approach to the theory of the elastic behaviour of multiphase materials. J Mech Phys Solids 11(2):127–140

Heise W, Ellis S (2016) On the coupling of geodynamic and resistivity models: a progress report and the way forward. Surv Geophys 37:81–107

Heise W, Bibby HM, Caldwell TG, Bannister SC, Ogawa Y, Takakura S, Uchida T (2007) Melt distribution beneath a young continental rift: the Taupo Volcanic Zone, New Zealand. Geophys Res Lett 34:L14313. doi:10.1029/2007GL029629

Herzberg C, Asimow PD, Arndt N, Niu Y, Lesher C, Fitton J, Cheadle M, Saunders A (2007) Temperatures in ambient mantle and plumes: constraints from basalts, picrites, and komatiites. Geochem Geophys Geosyst 8:Q02006. doi:10.1029/2006GC001390

Hinze E (1982) Laboratory electrical conductivity measurements on mantle relevant minerals. Geophys Surv 4:337–352

Hinze H, Will G, Cemic L (1981) Electrical conductivity measurements on synthetic olivines and on olivine, enstatite and diopside from Dreiser Weiher, Eifel (Germany) under defined thermodynamic activities as a function of temperature and pressure. Phys Earth Planet Inter 25:245–254

Hirschmann MM (2006) Water, melting, and the deep Earth H_2O cycle. Annu Rev Earth Planet Sci 34:629–653

Hirschmann MM, Aubaud C, Withers AC (2005) Storage capacity of H_2O in nominally anhydrous minerals in the upper mantle. Earth Planet Sci Lett 236:167–181

Hirschmann MM, Tenner T, Aubaud C, Withers A (2009) Dehydration melting of nominally anhydrous mantle: the primacy of partitioning. Phys Earth Planet Inter 176:54–68

Hirth G, Kohlstedt DL (1996) Water in the oceanic upper mantle: implications for rheology, melt extraction and the evolution of the lithosphere. Earth Planet Sci Lett 144:93–108

Ichiki M, Ogawa Y, Kaida T, Koyama T, Uyeshima M, Demachi T, Hirahara S, Honkura Y, Kanda W, Kono T (2015) Electrical image of subduction zone beneath northeastern Japan. J Geophys Res Solid Earth 120:7937–7965

Ionov D (2002) Mantle structure and rifting processes in the Baikal–Mongolia region: geophysical data and evidence from xenoliths in volcanic rocks. Tectonophysics 351:41–60

Irifune T, Ringwood AE (1987) Phase transformations in a harzburgite composition to 26 GPa: implications for dynamical behaviour of the subducting slab. Earth Planet Sci Lett 86:365–376
Jackson I, Fitz Gerald JD, Faul UH, Tan BH (2002) Grain-size-sensitive seismic wave attenuation in polycrystalline olivine. J Geophys Res 107(B12):2360. doi:10.1029/2001JB001225
Jackson I, Faul UH (2010) Grainsize-sensitive viscoelastic relaxation in olivine: towards a robust laboratory-based model for seismological application. Phys Earth Planet Inter 183:151–163
Jegen MD, Hobbs RW, Tarits P, Chave A (2009) Joint inversion of marine magnetotelluric and gravity data incorporating seismic constraints: preliminary results of sub-basalt imaging off the Faroe Shelf. Earth Planet Sci Lett 282:47–55
Jones AG (1999) Imaging the continental upper mantle using electromagnetic methods. In: van der Hilst RD, McDonough WF (eds) Developments in geotectonics. Elsevier, Amsterdam, pp 57–80
Jones AG (2016) Proton conduction and hydrogen diffusion in olivine: an attempt to reconcile laboratory and field observations and implications for the role of grain boundary diffusion in enhancing conductivity. Phys Chem Miner 43:237–265
Jones AG, Evans RL, Eaton DW (2009a) Velocity–conductivity relationships for mantle mineral assemblages in Archean cratonic lithosphere based on a review of laboratory data and Hashin–Shtrikman extremal bounds. Lithos 109:131–143
Jones AG, Evans RL, Muller MR, Hamilton MP, Miensopust MP, Garcia X, Cole P, Ngwisanyi T, Hutchins D, Fourie C (2009b) Area selection for diamonds using magnetotellurics: examples from Southern Africa. Lithos 112:83–92
Jones AG, Plomerova J, Korja T, Sodoudi F, Spakman W (2010) Europe from the bottom up: a statistical examination of the central and northern European lithosphere–asthenosphere boundary from comparing seismological and electromagnetic observations. Lithos 120:14–29
Jones AG, Fullea J, Evans RL, Muller MR (2012) Water in cratonic lithosphere: calibrating laboratory-determined models of electrical conductivity of mantle minerals using geophysical and petrological observations. Geochem Geophys Geosyst 13:Q06010. doi:10.1029/2012GC004055
Karato S (1990) The role of hydrogen in the electrical conductivity of the upper mantle. Nature 347:272–273
Karato S-I (2011) Water distribution across the mantle transition zone and its implications for global material circulation. Earth Planet Sci Lett 301:413–423
Karato S-I (2012) Deformation of earth materials: an introduction to the rheology of solid earth. Cambridge University Press, Cambridge
Karato S-I (2015) Some notes on hydrogen-related point defects and their role in the isotope exchange and electrical conductivity in olivine. Phys Earth Planet Inter 248:94–98
Karato S-I, Dai L (2009) Comments on "Electrical conductivity of wadsleyite as a function of temperature and water content" by Manthilake et al. Phys Earth Planet Inter 174:19–21
Karato S-I, Wang D (2013) Electrical conductivity of minerals and rocks. In: Karato S-I (ed) Physics and Chemistry of the deep earth. Wiley, Chichester. doi:10.1002/9781118529492.ch5
Karato S-I, Wu P (1993) Rheology of the upper mantle: a synthesis. Science 260:771–778
Katz RF, Spiegelman M, Langmuir CH (2003) A new parameterization of hydrous mantle melting. Geochem Geophys Geosyst 4(9):1073. doi:10.1029/2002GC000433
Kawakatsu H, Kumar P, Takei Y, Shinohara M, Kanazawa T, Araki E, Suyehiro K (2009) Seismic evidence for sharp lithosphere-asthenosphere boundaries of oceanic plates. Science 324:499–502
Kelbert A, Schultz A, Egbert G (2009) Global electromagnetic induction constraints on transition-zone water content variations. Nature 460:1003–1006
Kennett BLN, Jackson I (2009) Optimal equations of state for mantle minerals from simultaneous non-linear inversion of multiple datasets. Phys Earth Planet Inter 176:98–180. doi:10.1016/j.pepi.2009.04.005
Khan A (2016) On Earth's mantle constitution and structure from joint analysis of geophysical and laboratory-based data: an example. Surv Geophys 37:149–189
Khan A, Shankland T (2012) A geophysical perspective on mantle water content and melting: inverting electromagnetic sounding data using laboratory-based electrical conductivity profiles. Earth Planet Sci Lett 317:27–43
Khan A, Connolly JAD, Olsen N (2006) Constraining the composition and thermal state of the mantle beneath Europe from inversion of long-period electromagnetic sounding data. J Geophys Res 111:B10102. doi:10.1029/2006JB004270
Khan A, Connolly J, Maclennan J, Mosegaard K (2007) Joint inversion of seismic and gravity data for lunar composition and thermal state. Geophys J Int 168:243–258
Khan A, Zunino A, Deschamps F (2013) Upper mantle compositional variations and discontinuity topography imaged beneath Australia from Bayesian inversion of surface-wave phase velocities and thermochemical modeling. J Geophys Res 118:5285–5306. doi:10.1002/jgrb50304

Kind R, Yuan X, Saul J, Nelson D, Sobolev S, Mechie J, Zhao W, Kosarev G, Ni J, Achauer U (2002) Seismic images of crust and upper mantle beneath Tibet: evidence for Eurasian plate subduction. Science 298:1219–1221

Koch S, Kuvshinov A (2013) Global 3-D EM inversion of Sq variations based on simultaneous source and conductivity determination: concept validation and resolution studies. Geophys J Int 195(1):98–116

Kohlstedt DL, Mackwell SJ (1998) Diffusion of hydrogene and intrinsic point defects in olivine. Z Phys Chem 207:147–162

Kohlstedt D, Keppler H, Rubie D (1996) Solubility of water in the α, β and γ phases of (Mg, Fe) $2SiO_4$. Contrib Mineral Petrol 123:345–357

Korja T (2007) How is the European lithosphere imaged by magnetotellurics? Surv Geophys 28:239–272

Kovács I, Green DH, Rosenthal A, Hermann J, O'neill HSC, Hibberson WO, Udvardi B (2012) An experimental study of water in nominally anhydrous minerals in the upper mantle near the water-saturated solidus. J Petrol 53(10):2067–2093

Koyama T, Khan A, Kuvshinov A (2014) Three-dimensional electrical conductivity structure beneath Australia from inversion of geomagnetic observatory data: evidence for lateral variations in transition-zone temperature, water content and melt. Geophys J Int 196:1330–1350

Kozlovskaya E, Hjelt SE (2000) Modeling of elastic and electrical properties of solid–liquid rock system with fractal microstructure. Phys Chem Earth Part A 25:195–200

Kumar P, Yuan X, Kind R, Ni J (2006) Imaging the colliding Indian and Asian lithospheric plates beneath tibet. J Geophys Res 111:B06308. doi:10.1029/2005JB003930

Kuskov OL, Fabrichnaya OB (1994) Constitution of the Moon: 2. Composition and seismic properties of the lower mantle. Phys Earth Planet Inter 83(3–4):197–216

Kuskov O, Kronrod V, Prokofyev A, Pavlenkova N (2014) Thermo-chemical structure of the lithospheric mantle underneath the Siberian craton inferred from long-range seismic profiles. Tectonophysics 615:154–166

Kuvshinov A (2012) Deep electromagnetic studies from land, sea, and space: progress status in the past 10 years. Surv Geophys 33:169–209

Kuvshinov A, Junge A, Utada H (2006) 3-D modelling the electric field due to ocean tidal flow and comparison with observations. Geophys Res Lett 33:L06314. doi:10.1029/2005GL025043

Lallemant HA, Mercier JC, Carter N, Ross J (1980) Rheology of the upper mantle: inferences from peridotite xenoliths. Tectonophysics 70:85–113

Laštovičková, M (1991) A review of laboratory measurements of the electrical conductivity of rocks and minerals. Phys Earth Planet Inter 66(1-2):1–11

Laumonier M, Scaillet B, Pichavant M, Champallier R, Andujar J, Arbaret L (2014) On the conditions of magma mixing and its bearing on andesite production in the crust. Nat Commun 5:5607

Laumonier M, Farla R, Frost DJ, Katsura T, Marquardt K, Bouvier AS, Baumgartner LP (2017) Experimental determination of melt interconnectivity and electrical conductivity in the upper mantle. Earth Planet Sci Lett 463:286–297

Le Pape F, Jones AG, Unsworth MJ, Vozar J, Wei W, Jin S, Ye G, Jing J, Dong H, Zhang L (2015) Constraints on the evolution of crustal flow beneath Northern Tibet. Geochem Geophys Geosyst 16:4237–4260

Ledo J, Jones AG (2005) Upper mantle temperature determined from combining mineral composition, electrical conductivity laboratory studies and magnetotelluric field observations: application to the intermontane belt, Northern Canadian Cordillera. Earth Planet Sci Lett 236:258–268

Ledo J, Queralt P, Martí A, Jones AG (2002) Two-dimensional interpretation of three-dimensional magnetotelluric data: an example of limitations and resolution. Geophys J Int 150(1):127–139

Li Y-H, Wu Q-J, Tian X-B, Zeng R-S, Zhang R-Q, Li H-G (2006) Crustal structure beneath Qiangtang and Lhasa terrane from receiver function. Acta Seismol Sin 19:633–642

Liu C-Z, Wu F-Y, Chung S-L, Zhao Z-D (2011) Fragments of hot and metasomatized mantle lithosphere in Middle Miocene ultrapotassic lavas, southern Tibet. Geology 39:923–926

Love JJ, Rigler EJ (2014) The magnetic tides of Honolulu. Geophys J Int 197(3):1335–1353

Lu R, Keppler H (1997) Water solubility in pyrope to 100 kbar. Contrib Mineral Petrol 129:35–42

Mandolesi E, Jones AG (2014) Magnetotelluric inversion based on mutual information. Geophys J Int 199:242–252

Martí A (2014) The role of electrical anisotropy in magnetotelluric responses: from modelling and dimensionality analysis to inversion and interpretation. Surv Geophys 35(1):179–218

Matas J, Bass J, Ricard Y, Mattern E, Bukowinski MST (2007) On the bulk composition of the lower mantle: predictions and limitations from generalized inversion of radial seismic profiles. Geophys J Int 170:764–780. doi:10.1111/j.1365246X.2007.03454.x

Maus S, Kuvshinov A (2004) Ocean tidal signals in observatory and satellite magnetic measurements. Geophys Res Lett 31:L15313. doi:10.1029/2004GL020090
Maxwell-Garnett JCM (1904) Colours in metal glasses and in metallic films. Philos Trans R Soc Lond Ser A Contain Pap Math Phys Character 203:385–420
McDonough WF, Sun S-S (1995) The composition of the Earth. Chem Geol 120:223–253
Mierdel K, Keppler H, Smyth JR, Langenhorst F (2007) Water solubility in aluminous orthopyroxene and the origin of Earth's asthenosphere. Science 315:364–368
Miller KJ, Montési LG, Zhu WL (2015) Estimates of olivine–basaltic melt electrical conductivity using a digital rock physics approach. Earth Planet Sci Lett 432:332–341
Minster JB, Anderson DL (1981) A model of dislocation-controlled rheology for the mantle. Philos Trans R Soc Lond Ser A Math Phys Sci 299:319–356
Mookherjee M, Karato S-I (2010) Solubility of water in pyrope-rich garnet at high pressures and temperature. Geophys Res Lett 37:L03310
Moorkamp M, Jones AG, Eaton DW (2007) Joint inversion of teleseismic receiver functions and magnetotelluric data using a genetic algorithm: are seismic velocities and electrical conductivities compatible?. Geophys Res Lett 34:L16311. doi:10.1029/2007GL030519
Moorkamp M, Jones AG, Fishwick S (2010) Joint inversion of receiver functions, surface wave dispersion, and magnetotelluric data. J Geophys Res 115:B04318. doi:10.1029/2009JB006369
Mosenfelder JL, Deligne NI, Asimow PD, Rossman GR (2006) Hydrogen incorporation in olivine from 2 to 12 GPa. Am Mineral 91:285–294
Muller MR, Jones AG, Evans RL, Grütter HS, Hatton C, Garcia X, Hamilton MP, Miensopust MP, Cole P, Ngwisanyi T, Hutchins D, Fourie CJ, Jelsma HA, Evans SF, Aravanis T, Pettit W, Webb SJ, Wasborg J (2009) Lithospheric structure, evolution and diamond prospectivity of the Rehoboth Terrane and western Kaapvaal Craton, Southern Africa: constraints from broadband magnetotellurics. Lithos 112:93–105
Murch G (1983) The exact Nernst-Einstein equations and the interpretation of cross phenomenological coefficients in unary, binary, and ambipolar systems. Radiat Eff 73:299–305
Neska A (2016) Conductivity anomalies in central Europe. Surv Geophys 37:5–26
Ni H, Keppler H, Behrens H (2011) Electrical conductivity of hydrous basaltic melts: implications for partial melting in the upper mantle. Contrib Mineral Petrol 162:637–650
Novella D, Frost DJ, Hauri EH, Bureau H, Raepsaet C, Roberge M (2014) The distribution of H_2O between silicate melt and nominally anhydrous peridotite and the onset of hydrous melting in the deep upper mantle. Earth Planet Sci Lett 400:1–13
Novella D, Bolfan-Casanova N, Nestola F, Harris JW (2015) H_2O in olivine and garnet inclusions still trapped in diamonds from the Siberian craton: implications for the water content of cratonic lithosphere peridotites. Lithos 230:180–183
Nover G (2005) Electrical properties of crustal and mantle rocks—a review of laboratory measurements and their explanation. Surv Geophys 26:593–651
Olsen N, Friis-Christensen E, Floberghagen R, Alken P, Beggan CD, Chulliat A, Doornbos E, Da Encarnação JT, Hamilton B, Hulot G (2013) The Swarm satellite constellation application and research facility (SCARF) and Swarm data products. Earth Planets Space 65:1189–1200
Omura K, Kurita K, Kumazawa M (1989) Experimental study of pressure dependence of electrical conductivity of olivine at high temperatures. Phys Earth Planet Inter 57:291–303
Patterson M (1982) The determination of hydroxyl by infrared absorption in quartz, silicate glasses and similar minerals. Bull Mineral 105:20–29
Peslier AH (2010) A review of water contents of nominally anhydrous natural minerals in the mantles of Earth, Mars and the Moon. J Volcanol Geotherm Res 197:239–258
Peslier AH, Bizimis M (2015) Water in Hawaiian peridotite minerals: a case for a dry metasomatized oceanic mantle lithosphere. Geochem Geophys Geosyst 16:1211–1232
Peslier AH, Luhr JF (2006) Hydrogen loss from olivines in mantle xenoliths from Simcoe (USA) and Mexico: Mafic alkalic magma ascent rates and water budget of the sub-continental lithosphere. Earth Planet Sci Lett 242:302–319
Peslier AH, Luhr JF, Post J (2002) Low water contents in pyroxenes from spinel-peridotites of the oxidized, sub-arc mantle wedge. Earth Planet Sci Lett 201:69–86
Peslier AH, Woodland AB, Bell DR, Lazarov M (2010) Olivine water contents in the continental lithosphere and the longevity of cratons. Nature 467:78–81
Piazzoni AS, SteinleNeumann G, Bunge H-P, Dolejs D (2007) A mineralogical model for density and elasticity of the Earth's mantle. Geochem Geophys Geosyst 8:Q11010. doi:10.1029/2007GC001697
Pitzer KS, Sterner SM (1995) Equations of state valid continuously from zero to extreme pressures with H_2O and CO_2 as examples. Int J Thermophys 16:511–518

Poe BT, Romano C, Nestola F, Smyth JR (2010) Electrical conductivity anisotropy of dry and hydrous olivine at 8 GPa. Phys Earth Planet Inter 181:103–111
Pommier A (2014) Interpretation of magnetotelluric results using laboratory measurements. Surv Geophys 35:41–84
Pommier A, Gaillard F, Pichavant M, Scaillet B (2008) Laboratory measurements of electrical conductivities of hydrous and dry Mount Vesuvius melts under pressure. J Geophys Res 113:B05205
Pommier A, Leinenweber K, Kohlstedt DL, Qi C, Garnero EJ, Mackwell SJ, Tyburczy JA (2015) Experimental constraints on the electrical anisotropy of the lithosphere-asthenosphere system. Nature 522(7555):202–206
Püthe C, Kuvshinov A (2014) Mapping 3-D mantle electrical conductivity from space: a new 3-D inversion scheme based on analysis of matrix Q-responses. Geophys J Int 197:768–784
Ricard Y, Mattern E, Matas J (2005) Synthetic tomographic images of slabs from mineral physics, Washington DC. Am Geophys Union Geophys Monogr Ser 160:283–300. doi:10.1029/160GM17
Ringwood AE (1975) Composition and petrology of the earth's mantle/A. E. Ringwood. McGraw-Hill, New York
Romano C, Poe BT, Kreidie N, McCammon CA (2006) Electrical conductivities of pyrope–almandine garnets up to 19 GPa and 1700 °C. Am Mineral 91:1371–1377
Roux E, Moorkamp M, Jones AG, Bischoff M, Endrun B, Lebedev S, Meier T (2011) Joint inversion of long-period magnetotelluric data and surface-wave dispersion curves for anisotropic structure: application to data from central Germany. Geophys Res Lett 38:L05304. doi:10.1029/2010GL046358
Sabaka TJ, Olsen N, Purucker ME (2004) Extending comprehensive models of the Earth's magnetic field with Ørsted and CHAMP data. Geophys J Int 159:521–547
Sabaka TJ, Tyler RH, Olsen N (2016) Extracting ocean-generated tidal magnetic signals from Swarm data through satellite gradiometry. Geophys Res Lett 43:3237–3245
Sakurai M, Tsujino N, Sakuma H, Kawamura K, Takahashi E (2014) Effects of Al content on water partitioning between orthopyroxene and olivine: implications for lithosphere–asthenosphere boundary. Earth Planet Sci Lett 400:284–291
Schmerr N (2012) The Gutenberg discontinuity: melt at the lithosphere-asthenosphere boundary. Science 335:1480–1483
Schnepf NR, Manoj C, Kuvshinov A, Toh H, Maus S (2014) Tidal signals in ocean-bottom magnetic measurements of the Northwestern Pacific: observation versus prediction. Geophys J Int 198(2):1096–1110
Schnepf N, Kuvshinov A, Sabaka T (2015) Can we probe the conductivity of the lithosphere and upper mantle using satellite tidal magnetic signals? Geophys Res Lett 42:3233–3239
Schock RN, Duba A, Shankland TJ (1989) Electric conduction in olivine. J Geophys Res 94:5829–5839
Schulgasser K (1976) Relationship between single-crystal and polycrystal electrical conductivity. J Appl Phys 47:1880–1886
Schulgasser K (1977) Bounds on the conductivity of statistically isotropic polycrystals. J Phys C: Solid State Phys 10:407–417
Seifert KF, Will G, Voigt R (1982) Electrical conductivity measurements on synthetic pyroxenes $MgSiO_3$–$FeSiO_3$ at high pressures and temperatures under defined thermodynamic conditions. In: Schreyer W (ed) High-pressure researches in geoscience. Schweizerbart'sche, Sttutgart, pp 419–432
Selway K, Yi J, Karato S-I (2014) Water content of the Tanzanian lithosphere from magnetotelluric data: implications for cratonic growth and stability. Earth Planet Sci Lett 388:175–186
Semenov A, Kuvshinov A (2012) Global 3-D imaging of mantle conductivity based on inversion of observatory C-responses: II. Data analysis and results. Geophys J Int 191:965–992
Shapiro N, Ritzwoller M (2004) Thermodynamic constraints on seismic inversions. Geophys J Int 157(3):1175–1188
Shimizu H, Koyama T, Baba K, Utada H (2010) Revised 1-D mantle electrical conductivity structure beneath the north Pacific. Geophys J Int 180:1030–1048
Sifré D, Gardés E, Massuyeau M, Hashim L, Hier-Majumder S, Gaillard F (2014) Electrical conductivity during incipient melting in the oceanic low-velocity zone. Nature 509:81–85
Simmons NA, Forte AM, Boschi L, Grand SP (2010) GyPSuM: a joint tomographic model of mantle density and seismic wave speeds. J Geophys Res 115:B12310. doi:10.1029/2010JB007631
Siripunvaraporn W (2012) Three-dimensional magnetotelluric inversion: an introductory guide for developers and users. Surv Geophys 33:5–27
Sobolev SV, Zeyen H, Stoll G, Werling F, Altherr R, Fuchs K (1996) Upper mantle temperatures from teleseismic tomography of French Massif Central including effects of composition, mineral reactions, anharmonicity, anelasticity and partial melt. Earth Planet Sci Lett 139:147–163

Spangenberg E (1998) A fractal model for physical properties of porous rock: theoretical formulations and application to elastic properties. J Geophys Res 103:12269–12289
Spichak VV, Zakharova OK, Goidina AG (2013) A new conceptual model of the Icelandic crust in the Hengill geothermal area based on the indirect electromagnetic geothermometry. J Volcanol Geotherm Res 257:99–112
Stixrude L, Lithgow-Bertelloni C (2005) Thermodynamics of mantle minerals—I. Physical properties. Geophys J Int 162:610–632
Stixrude L, Lithgow-Bertelloni C (2011) Thermodynamics of mantle minerals—II. Phase equilibria. Geophys J Int 184:1180–1213
Tarits P, Mandéa M (2010) The heterogeneous electrical conductivity structure of the lower mantle. Phys Earth Planet Inter 183:115–125
ten Grotenhuis SM, Drury MR, Peach CJ, Spiers CJ (2004) Electrical properties of fine-grained olivine: evidence for grain boundary transport. J Geophys Res 109:B06203. doi:10.1029/2003JB002799
Tenner TJ, Hirschmann MM, Withers AC, Ardia P (2012) H_2O storage capacity of olivine and low-Ca pyroxene from 10 to 13 GPa: consequences for dehydration melting above the transition zone. Contrib Mineral Petrol 163:297–316
Thiel S, Heinson G (2013) Electrical conductors in Archean mantle—Result of plume interaction? Geophy Res Lett 40(12):2947–2952
Toffelmier DA, Tyburczy JA (2007) Electromagnetic detection of a 410-km-deep melt layer in the southwestern United States. Nature 447:991–994
Tyburczy JA, Waff HS (1983) Electrical conductivity of molten basalt and andesite to 25 kilobars pressure: geophysical significance and implications for charge transport and melt structure. J Geophys Res 88:2413–2430
Velímský J (2013) Determination of three-dimensional distribution of electrical conductivity in the Earth's mantle from Swarm satellite data: time-domain approach. Earth Planets Space 65:1239–1246
Verhoeven O et al (2009) Constraints on thermal state and composition of the Earths lower mantle from electromagnetic impedances and seismic data. J Geophys Res 114:B03302. doi:10.1029/2008JB005678
Vozar J, Jones AG, Fullea J, Agius MR, Lebedev S, Le Pape F, Wei W (2014) Integrated geophysical–petrological modeling of lithosphere-asthenosphere boundary in central Tibet using electromagnetic and seismic data. Geochem Geophys Geosyst 15:3965–3988
Waff HS (1974) Theoretical considerations of electrical conductivity in a partially molten mantle and implications for geothermometry. J Geophys Res 79:4003–4010
Wang Z, Ji S, Dresen G (1999) Hydrogen-enhanced electrical conductivity of diopside crystals. Geophys Res Lett 26:799–802
Wang D, Mookherjee M, Xu Y, Karato S-I (2006) The effect of water on the electrical conductivity of olivine. Nature 443:977–980
Wannamaker PE (2005) Anisotropy versus heterogeneity in continental solid earth electromagnetic studies: fundamental response characteristics and implications for physicochemical state. Surv Geophys 26(6):733–765
Withers AC, Wood BJ, Carroll MR (1998) The OH content of pyrope at high pressure. Chem Geol 147:161–171
Xia Q-K, Sheng Y-M, Yang X-Z, Yu H-M (2005) Heterogeneity of water in garnets from UHP eclogites, eastern Dabieshan, China. Chem Geol 224:237–246
Xu Y, Shankland TJ (1999) Electrical conductivity of orthopyroxene and its high pressure phases. Geophys Res Lett 26:2645–2648
Xu Y, Shankland TJ, Poe BT (2000) Laboratory-based electrical conductivity in the Earth's mantle. J Geophys Res 105:27865–27875
Xu W, Lithgow-Bertelloni C, Stixrude L, Ritsema J (2008) The effect of bulk composition and temperature on mantle seismic structure. Earth Planet Sci Lett 275:70–79
Yang X, McCammon C (2012) Fe^{3+}-rich augite and high electrical conductivity in the deep lithosphere. Geology 40:131–134
Yang Y, Ritzwoller MH, Lin F-C, Moschetti MP, Shapiro NM (2008) Structure of the crust and uppermost mantle beneath the western United States revealed by ambient noise and earthquake tomography. J Geophys Res 113:B12310. doi:10.1029/2008JB005833
Yang X, Keppler H, McCammon C, Ni H, Xia Q, Fan Q (2011) Effect of water on the electrical conductivity of lower crustal clinopyroxene. J Geophys Res 116:B04208. doi:10.1029/2010JB008010
Yang X, Keppler H, McCammon C, Ni H (2012) Electrical conductivity of orthopyroxene and plagioclase in the lower crust. Contrib Mineral Petrol 163:33–48

Yoshino T (2010) Laboratory electrical conductivity measurement of mantle minerals. Surv Geophys 31:163–206
Yoshino T, Katsura T (2012) Re-evaluation of electrical conductivity of anhydrous and hydrous wadsleyite. Earth Planet Sci Lett 337:56–67
Yoshino T, Katsura T (2013) Electrical conductivity of mantle minerals: role of water in conductivity anomalies. Annu Rev Earth Planet Sci 41:605–628
Yoshino T, Manthilake G, Matsuzaki T, Katsura T (2008a) Dry mantle transition zone inferred from the conductivity of wadsleyite and ringwoodite. Nature 451:326–329
Yoshino T, Nishi M, Matsuzaki T, Yamazaki D, Katsura T (2008b) Electrical conductivity of majorite garnet and its implications for electrical structure in the mantle transition zone. Phys Earth Planet Inter 170:193–200
Yoshino T, Matsuzaki T, Shatskiy A, Katsura T (2009) The effect of water on the electrical conductivity of olivine aggregates and its implications for the electrical structure of the upper mantle. Earth Planet Sci Lett 288:291–300
Yoshino T, Laumonier M, McIsaac E, Katsura T (2010) Electrical conductivity of basaltic and carbonatite melt-bearing peridotites at high pressures: implications for melt distribution and melt fraction in the upper mantle. Earth Planet Sci Lett 295:593–602
Yuan H, Romanowicz B (2010) Lithospheric layering in the North American craton. Nature 466:1063–1068
Yue H, Chen YJ, Sandvol E, Ni J, Hearn T, Zhou S, Feng Y, Ge Z, Trujillo A, Wang Y (2012) Lithospheric and upper mantle structure of the northeastern Tibetan Plateau. J Geophys Res 117:B5. doi:10.1029/2011JB008545
Zhang B, Yoshino T, Wu X, Matsuzaki T, Shan S, Katsura T (2012) Electrical conductivity of enstatite as a function of water content: implications for the electrical structure in the upper mantle. Earth Planet Sci Lett 357:11–20
Zhang B, Yoshino T, Yamazaki D, Manthilake G, Katsura T (2014) Electrical conductivity anisotropy in partially molten peridotite under shear deformation. Earth Planet Sci Lett 405:98–109
Zhao W, Mechie J, Brown L, Guo J, Haines S, Hearn T, Klemperer S, Ma Y, Meissner R, Nelson K (2001) Crustal structure of central Tibet as derived from project INDEPTH wide-angle seismic data. Geophys J Int 145:486–498
Zhao Y-H, Ginsberg SB, Kohlstedt DL (2004) Solubility of hydrogen in olivine: dependence on temperature and iron content. Contrib Mineral Petrol 147:155–161
Zunino A, Khan A, Cupillard P, Mosegaard K (2016) Constitution and structure of Earth's mantle: insights from mineral physics and seismology. In: Moorkamp M, Lelievre P, Linde N, Khan A (eds) Integrated imaging of the Earth. AGU Monograph, Wiley, Hoboken